Multiple Mantle Melting and Metasomatism during the Initial Stages of Subduction: Multi-Geochemical and Os-Isotope Evidence from Well-Preserved Kızıldağ Ophiolite, southern Türkiye

Ibrahim Uysal, Ahmet Şen, Ben-Xun Su, Yalçin Ersoy, Yilmaz Demir, Qi-Qi Pan, Wen-Jun Hu, Utku Bağci, Marguerite Godard

To cite this version:

Ibrahim Uysal, Ahmet Şen, Ben-Xun Su, Yalçin Ersoy, Yilmaz Demir, et al.. Multiple Mantle Melting and Metasomatism during the Initial Stages of Subduction: Multi-Geochemical and Os-Isotope Evidence from Well-Preserved Kızıldağ Ophiolite, southern Türkiye. Journal of Petrology, 2025, 66 (8), pp.egaf066. ⟨10.1093/petrology/egaf066⟩. ⟨hal-05269684⟩

HAL Id: hal-05269684
https://hal.science/hal-05269684v1

Submitted on 8 Oct 2025

Multiple mantle melting and metasomatism during the initial stages of subduction: Multi-geochemical and Os-isotope evidence from well-preserved Kızıldağ ophiolite, S Türkiye

Ibrahim Uysal[1,2*], Ahmet D. Şen[3], Ben-Xun Su[2], Yalçın Ersoy[4], Yılmaz Demir[5], Qi-Qi Pan[2], Wen-Jun Hu[6], Utku Bağcı[7], Marguerite Godard[8]

[1]Karadeniz Technical University, Department of Geological Engineering, Trabzon, Türkiye

[2]State Key Laboratory of Lithospheric and Environmental Coevolution, Institute of Geology and Geophysics, Chinese Academy of Sciences, Beijing 100029, China

[3]Gümüşhane University, Department of Geological Engineering, Gümüşhane, Türkiye

[4]Dokuz Eylül University, Department of Geological Engineering, İzmir, Türkiye

[5]Recep Tayyip Erdoğan University, Department of Geological Engineering, Rize, Türkiye

[6]State Key Laboratory of Critical Mineral Research and Exploration, Institute of Geochemistry, Chinese Academy of Sciences, Guiyang 550081, China

[7]Mersin University, Department of Geological Engineering, Mersin, Türkiye

[8]Géosciences Montpellier, Université de Montpellier, CNRS, Montpellier, France

*Corresponding author:

Ibrahim Uysal (iuysal@ktu.edu.tr; uysal.ibrahim@gmail.com)

Abstract

The processes governing ophiolite formation and evolution remain incompletely understood. The Kızıldağ ophiolite, a well-preserved remnant of the Neo-Tethyan oceanic lithosphere in the Anatolian region, offers critical insights into subduction-related processes and geodynamics. This study presents new element data for mineral and whole-rock samples, combined with Re-Os isotopic compositions of mantle peridotites and associated crustal rocks and extrusives. Petrographic observations identify two distinct groups of peridotites: (i) those with very low modal clinopyroxene, interpreted as highly depleted harzburgitesand preserving primary mineral assemblages, and (ii) depleted harzburgites containing secondary clinopyroxene with elevated trace element contents, inferred to have crystallized from percolating melts and thus reflecting metasomatic modification. Spinel and orthopyroxene compositions indicate 17 to 25% degrees of partial melting, with evidence for melting in both garnet and spinel stability fields. However, mineral and whole-rock compositions also record subsequent cryptic and modal metasomatism. Crustal rocks and extrusives exhibit geochemical signatures transitional between fore-arc basalts and boninites, consistent with subduction initiation settings. Variations in Os isotope ratios ($^{187}Os/^{188}Os$) in crustal rocks further reveal melt-rock interactions and the incorporation of radiogenic Os from subducted oceanic crust.

The integration of petrographic, geochemical, and isotopic data supports a four-stage tectonic model for subduction initiation and mantle wedge evolution, consistent with global models proposed for supra-subduction zone (SSZ) ophiolites, particularly those of the Tethyan domain. These findings provide new constraints on mantle melting, metasomatism, and subduction initiation processes and contribute to a broader understanding of SSZ mantle evolution in both regional and global contexts.

Keywords: Kızıldağ ophiolite; Mantle metasomatism; Partial melting; OphioliSubduction initiation

Introduction

The formation and evolution of oceanic lithosphere in supra-subduction zone (SSZ) environments represent a complex interplay of mantle melting, melt extraction, and melt-rock interactions, significantly influenced by slab-derived fluids and dehydration reactions. These processes distinguish SSZ settings from mid-ocean ridge (MOR) environments by introducing hydrous melting, metasomatism, and enhanced melt productivity in the mantle wedge (e.g., Arai et al., 2006; Batanova et al., 2011; Lissenberg et al., 2013; Coogan et al., 2020; Su et al., 2023). Understanding these dynamic processes is crucial for deciphering the intricate workings of plate tectonics and their influence on global geochemical cycles (Zhang et al., 2024). Mantle peridotites, the residual mantle after melt extraction, serve as invaluable recorders of these processes. In SSZs, these peridotites are typically the residues of significant partial melting (generally exceeding 15%), often undergoing extensive metasomatism by diverse melts and fluids derived from the subducting slab (e.g., Arai, 1994; Parkinson and Pearce, 1998). This complex history leaves a distinctive geochemical imprint on the mantle wedge, making it a critical focus for understanding the interplay between mantle dynamics and subduction processes. The pervasive alteration, including serpentinization, commonly observed in SSZ peridotites (Parkinson et al., 1992; Ishii et al., 2000; Pearce et al., 2000), further complicates geochemical interpretations. Therefore, a rigorous and multifaceted approach integrating multiple-mineral phase data, advanced analytical techniques, and detailed petrographic observations is essential for robust interpretations of both partial melting and subsequent metasomatism events (e.g., Zhou et al., 2005; Uysal et al., 2007, 2012, 2014; Jean et al., 2010; Scott et al., 2016; Jean and Shervais, 2017). However, the complex interactions between melt transport (through both diffuse porous flow and focused conduits) and mantle minerals profoundly influence upper mantle chemistry and mineralogy (e.g., Warren, 2016; Rampone et al., 2020; Borghini et al., 2023; Su et al., 2023), generating substantial chemical and isotopic heterogeneities that reflect the highly dynamic nature of mantle processes. Clinopyroxene, for instance, is commonly used to estimate the degree of partial melting and to infer theectonic environment based on its trace element compositions (Johnson and Dick, 1992; Hellebrand et al., 2002). In depleted mantle rocks, clinopyroxene is typically present in low modal abundance and small grain sizes due to its early melting. These small grains are highly susceptible to modification by percolating melts of varying compositions, which can obscure the original geochemical information related to partial melting. In contrast, orthopyroxene, which is coarser-grained than both clinopyroxene and spinel in mantle peridotites, is more resistant to alteration. Particularly, the core of larger orthopyroxene grains is more likely to retain its original composition and escape metasomatism, allowing for better preservation of primary geochemical signatures. This characteristic makes orthopyroxene a more reliable indicator of the conditions under which mantle peridotites formed.

Most of the Tethyan ophiolites within the Alpine, Mediterranean and Tibetan-Himalayan orogenic belts offer an opportunity to investigate these complex SSZ interactions (see Dilek and Furnes, 2019). Among them, the Kızıldağ ophiolite in Anatolia (Fig. 1) is an exceptionally well-preserved remnant of the Neo-Tethyan oceanic lithosphere and exhibits a nearly complete sequence, extending from mantle peridotites to volcanic extrusives, a feature rarely observed in other ophiolites. The readily accessible nature of the ophiolite, particularly along the ~20 km road between Kale to the NW and Çevlik to the SE, enabled systematic sampling across the Moho transition zone, from deeper mantle to cumulate gabbros and sheeted dikes, providing an unparalleled dataset. The crustal rocks and extrusives of the Kızıldağ ophiolite have been extensively studied by various researchers (Lytwyn and Casey, 1993; Dilek and Thy, 1998; Bağcı et al., 2005; Chen et al., 2019, 2020; Şimşek et al., 2023; Su et al., 2025). Dilek and Thy (1998) and Bağcı et al. (2008) proposed a SSZ origin for the ophiolite based on the major and trace element compositions of the cumulate rocks. Furthermore, recent studies on mantle peridotites have indicated a multi-stage origin for the Kızıldağ ophiolite during the subduction initiation (Uysal et al., 2012; Chen et al., 2019; Aldanmaz et al., 2020; Lin et al., 2020; Su et al., 2025). However, a comprehensive understanding of its petrogenesis, encompassing both mantle and crustal sections and the full spectrum of magmatic and metasomatic processes, remains elusive. This necessitates a detailed investigation of both the mantle and crustal sections to fully resolve the complexities of its formation and evolution within the context of subduction initiation models. Furthermore, the integration of various geochemical proxies, including trace element concentrations of clinopyroxene and orthopyroxene as well as high-precision highly siderophile elements (HSE) and Os isotope data, is crucial for obtaining a more complete and nuanced understanding of the petrogenetic processes.

This study presents a novel, integrated dataset to address these knowledge gaps. Our multi-faceted analytical approach combines whole-rock major and trace element analyses, detailed mineral chemistry (spinel, olivine, orthopyroxene, clinopyroxene, amphibole, plagioclase), and high-precision analyses of highly siderophile elements (HSE: Os, Ir, Ru, Pt, Pd, Re, Au) and Os isotope data. This comprehensive dataset, coupled with the strategic sampling approach across the entire ophiolite sequence, enables a detailed characterization of compositional variations and provides a robust framework for elucidating the petrogenetic processes involved in subduction initiation. Our analysis focuses on three primary objectives: 1) refining estimates of the degree of partial melting using a multi-proxy approach (whole-rock, spinel, orthopyroxene) and proposing a novel two-stage garnet + spinel melting model for the Kızıldağ mantle peridotites; 2) thoroughly characterizing the nature of metasomatic events by analyzing variations in major and trace element abundances as well as Os isotope compositions, focusing on the influence of subduction-related fluids and melts; and 3) rigorously testing existing subduction initiation models by comparing our findings with the extensive geochemical database from the well-studied Oman ophiolite, specifically evaluating the relative contributions of fore-arc basaltic and boninitic magmatisms during subduction initiation. This integrated approach is expected to provide significant new constraints on formation of oceanic lithosphere in SSZ settings and crucial insights into the processes that shape subduction zone magmatism and mantle dynamics. The results will contribute to a more complete understanding of the complex interplay between mantle melting, melt extraction, and metasomatism in SSZ environments, particularly within the context of subduction initiation.

Geological setting and field observations

The eastern Mediterranean's Tethyan ophiolites, remnants of the ancient Tethys oceans, occur in several east-west belts interspersed with continental fragments and basins north of the Arabian Peninsula. Obduction during the Late Cretaceous, resulting from arc-trench collisions with continental margins (Dilek et al., 1999; Dilek and Thy, 2009), was followed by subduction and final continental collision by the middle-late Eocene (Dilek and Moores, 1990). The Kızıldağ ophiolite, situated in the Bitlis-Zagros suture zone of southeastern Türkiye (Fig. 1), serves as a key example in this context. Its formation within a Late Cretaceous arc-trench system along the northern Arabian margin (Dilek and Thy, 2009) is supported by zircon U-Pb ages (~91-94 Ma), which are consistent with other Tethyan ophiolites (Mukasa and Ludden, 1987; Chan et al., 2007), indicating a regionally extensive arc-trench system (Dilek and Flower, 2003). Obduction onto the Arabian margin, biostratigraphically constrained to the post-Turonian (90 Ma) and pre-Maastrichtian (71 Ma) (Dilek and Thy, 2009), correlates with broader Late Cretaceous Tethyan obduction events linked to Tethys closure and the formation of the present-day Eurasian-African-Arabian plate configuration (Dewey et al., 1986; Dilek and Moores, 1990).

The Kızıldağ ophiolite is one of the best-preserved remnants of the Neo-Tethyan oceanic lithosphere, thrust onto the NW Arabian plate during the late Cretaceous period. Following the emplacement of the ophiolite, Maastrichtian-aged cover sediments were deposited, sealing the obduction thrust (Karaoğlan et al., 2013; Maffione et al., 2017). The main body of the ophiolite extends approximately 45 km in a NE-SW direction along the eastern Mediterranean coast and consists of a mantle peridotite core (Fig. 1b) (Bağcı et al., 2005; Dilek and Thy, 2009; Karaoğlan et al., 2013). To the southeast, this core is overlain by a sequence of plutonic rocks and a sheeted dike complex. In the northwest, isolated fault blocks of plutonic and dike rocks crop out adjacent to the peridotite core. Gently dipping normal faults create contacts between the peridotite and plutonic units in both the northwest and southeast, forming well-developed low-angle shear zones (Fig. 1b, d). In the northeastern section, the ophiolite lacks the internal structure and stratigraphy found in the main massif. This area consists of volcanic, dike, and plutonic rocks directly overlying the serpentinized peridotites, with faulted contacts often forming down-dropped hanging wall blocks (Dilek and Delaloye, 1992). The mantle section of the ophiolite, locally exceeding 3 km in thickness and predominantly composed of harzburgites, is intruded by pegmatitic gabbro and pyroxenite veins, as well as rodingite veins (Fig. 1c3; Pişkin et al., 1990; Dilek and Thy, 1998; Bağcı et al., 2005). Throughout the peridotite massif, pods of dunite and chromitite bodies are also present. Serpentinization is widespread, often masking the primary igneous mineralogy and metamorphic structures within these harzburgites. These harzburgites typically exhibit a brownish color due to weathering on their outer surfaces, while their fresh cores display dark green to gray hues. Orthopyroxene is readily observable on the fresh core surfaces of harzburgite samples that have experienced minimal serpentinization. Poikilitic ultramafic cumulates, situated between the underlying mantle peridotite and the overlying gabbros and sheeted dikes in fault contact (Dilek and Delaloye, 1992), are exposed in both northern and southern sections beneath these lithologies (Fig. 1). The lower portion of the gabbroic sequence is characterized by layered gabbros, while the upper level predominantly features fine-grained isotropic gabbros. Plastic deformation bands and crosscutting intrusive contacts suggest that these cumulate rocks underwent multiple stages of syn-magmatic extension and crustal accretion (Dilek and Thy, 2009). The sheeted dike complex and the extrusive sequence form the roof of the ophiolite body (Bağcı et al., 2005; Dilek and Thy, 2009). In addition, plagiogranite is found intruding into the upper part of the isotropic gabbros in the Karaçay valley and at the contact with the sheeted dike complex in Çevlik area (Bağcı et al., 2008). Remarkably, this entire section, extending from the mantle to the uppermost crust, is accessible along a 20 km stretch of road between Kale to the northwest and Çevlik to the southeast (Fig. 1a). Within the crustal portion of the Kızıldağ ophiolite, two distinct volcanic extrusives have been identified: (i) low-K tholeiite volcanic rocks, primarily located near Kömürçukuru and (ii) boninite-like compositions found in the southern section of the ophiolite body near the southeastern region of Hatay city. These volcanic rocks, along with sheeted dikes and isotropic gabbros, exhibit basaltic to basaltic andesite compositions, indicating a range of magmatic sources from island arc tholeiite to boninite (Dilek and Thy, 1998, 2009; Bağcı et al., 2005, 2008; Liu et al., 2020).

Analytical methods

Whole-rock major oxide analyses of samples from the Kızıldağ ophiolite were performed at ACME Analytical Laboratory in Vancouver (Canada) using X-ray fluorescence. To ensure the data quality of the major element analyses, an intralab standard, Reference Material STD-SO-18, was evaluated alongside the samples. The results indicated that relative standard deviations (RSD) for most major elements were at or below 1%. However, for Cr and Mn, the RSD were slightly higher, recorded at 1.8% and 1.3%, respectively. The loss on ignition was determined by heating 0.5 g of rock powder from each sample at 1000 °C for 5 hours. Trace element concentrations were measured using Inductively Coupled Plasma Mass Spectrometry (ICP-MS) with a Thermo Scientific X-Series2 apparatus in the Department of Earth Sciences at the University of Durham, UK. This analysis followed a standard nitric and hydrofluoric acid digestion procedure to ensure comprehensive extraction of the elements. The detailed analytical procedure for sample preparation is given in Ottley et al. (2003). Calibration of the ICP-MS data was achieved using international rock standards (BHVO-1, AGV-1, W-2, NBS688) alongside an in-house peridotite standard (GP13) (Ottley et al., 2003). The aforementioned standards and analytical blanks were prepared using the same technique as the samples to ensure consistency. To enhance the signal-to-noise ratio for low-abundance isotopes, the instrument dwell times were increased (Ottley et al., 2003). The compositions of the reference samples (W-2, AGV-1, BHVO-1, BE-N, and NBS688) were analyzed as unknowns alongside the Kızıldağ samples during the same analytical runs. For the analyzed trace elements, the reproducibility (RSD) of the in-house peridotite standard is generally better than 2%, and the measured compositions are in good agreement with the values reported in Potts et al. (1992). Detection limits for each major and trace element, average blank values, as well as the averages, standard deviations, and RSD values for the reference material STD SO-18 for major oxides and the in-house peridotite standard (GP13) for trace elements are provided in Supplementary Table 1a.

Specific areas of peridotite sampels were examined using the TESCAN Integrated Mineral Analyzer (TIMA) at the Institute of Geochemistry, Chinese Academy of Sciences (IGCAS). The analyses were conducted at a voltage of 25 kV and a current of 8.8 nA, with a working distance of 15 mm and a pixel size of 1 μm.

Mineral chemistry analyses were conducted at the Department of Earth and Environmental Sciences, LMU Munich (Munich, Germany), utilizing a Cameca SX-100 electron microprobe equipped with a LaB6 cathode. Data are given in Supplementary Table 2. Measurements were performed with wavelength-dispersive spectrometers at 15 kV and 20 nA, employing counting times of 10 to 30 seconds for silicates (30 seconds for Al, Ni, and Ca; 20 seconds for Ti; and 10 seconds for all other elements). The beam size was fixed at 1 μm. For chromian spinel, counting times of 100 seconds for Ti, 30 seconds for Ni, and 10 seconds for all other elements were implemented to reduce the detection limits of Ti. The following standards were used for calibration: wollastonite (Si, Ca); Al_2O_3 (Al); Fe_2O_3 (Fe); Cr_2O_3 (Cr);

rutile (Ti); bustamite (Mn); NiO (Ni); periclase (Mg); albite (Na); and orthoclase (K). Calibration was checked and redone prior to analyses and again after analyses on the used standards, noting that no drift was observed. Background measurements were taken on two sides of the peak, which were used to calculate a linear background correction for the peak position. Raw data were corrected using the PAP matrix correction method (Pouchou and Pichoir, 1984).The software used for data reduction was PeakSight, provided by Cameca. The amount of Fe^{3+} in the chromian spinel was calculated based on the ideal stoichiometry of chromian spinel, represented as $A^{2+}B^{3+}_2O_4$, with specific consideration of the iron valence state through stoichiometric calculations.

Mineral trace element compositions were determined at Montpellier University (France) using two different ICP-MS coupled with a laser ablation (LA) system. The Geolas automated platform, equipped with a 193 nm Compex 102 laser from LambdaPhysik, was employed for the analyses. Clinopyroxenes and orthopyroxenes were analyzed using a ThermoFinnigan Element 2 High Resolution-ICP-MS (HR-ICP-MS) instrument with a single collector double-focusing sector field, the Element XR (Extended Range). Data are provided in Supplementary Tables 3 and 4. Prior to analysis, the carbon coating on thick samples was removed. The sample particles were mixed with argon in a cell filled with helium gas before being introduced into the plasma. Signals were acquired in Time Resolved Acquisition mode, with 2 minutes allocated for the blank measurements and 1 minute for analyses of the NIST 612 certified reference material. The laser operated at a frequency of 8 Hz with a spot size of 163 µm for clinopyroxene and orthopyroxene analyses on the HR-ICP-MS. Oxide levels, measured using the ThO/Th ratio, were kept below 0.7%. Internal standards of ^{43}Ca and ^{29}Si were used for analyses, with concentrations calibrated against the NIST 612 rhyolitic glass, following the values provided by Pearce et al. (1997). Data processing was conducted using GLITTER software, applying the linear fit to ratio method, which yielded a precision of 5 to 10% (1 sigma) for most analyses as determined by multiple runs of reference basalt (BIR-1G). The detection limits for clinopyroxene and orthopyroxene were below 0.1 µg/g for all elements except Zr, Ti, V, Cr, and Ni (which ranged from 0.2 to 6 µg/g) for LA-ICP-MS, and below 0.02 µg/g for all elements except V, Cr, Co, Zn, Rb, Sr, and Ba (which ranged from 0.03 to 0.3 µg/g), as well as Ti, Ni, and Zn (which ranged from 2 to 4 µg/g) for LA-HR-ICP-MS.

The analysis of Os isotope ratios for 14 selected samples was conducted at the University of Tübingen in Mannheim, Germany, with data presented in Supplementary Table 5. Osmium was analyzed using negative thermal ionization mass spectrometry (NTI-MS) with electron bombardment mode on platinum (Pt) filaments using the Thermo Finnigan Triton instrument (Creaser et al., 1991; Volkening et al., 1991). The reanalysis of the reference solution (UMd) from the University of Maryland, which contained 1.75 pg of ^{187}Os and 17 pg of ^{188}Os, was performed at Durham University between October 2005 and November 2011, yielding an $^{187}Os/^{188}Os$ ratio of 0.11378 ± 0.28 (2σ). For larger solutions (>10 ng), the same instrument in Faraday cup mode determined this ratio as 0.113787 ± 0.07 (Luguet et al., 2008). For whole-rock Re-Os analyses, the blank values for Os ranged from 0.04 to 0.51 pg (average: 0.21 pg), while the blank values for $^{187}Os/^{188}Os$ ratios varied from 0.140 to 0.675 (average: 0.32). The blank value for Re ranged from 0.3 to 9 pg (average: 1.6 pg). The reproducibility of osmium measurements is typically around ±10% or better.

The analysis of platinum-group elements (PGE; Ir, Ru, Rh, Pt, Pd) and Au in the samples was carried out at the Geoscience Laboratory in Ontario, Sudbury, Canada. For this analysis, a 25 g sample was melted with a flux mixture of borax, soda ash, silica, nickel oxide, and sulfur. The melt was held at 1200 °C to ensure complete fusion and retention of all PGE and Au in the form of nickel sulfide. The nickel sulfide button was subsequently dissolved in hydrochloric acid at approximately 100 °C. Afterward, insoluble PGE and Au sulfides were collected on a cellulose nitrate membrane filter and digested in a borosilicate test tube in a floating state. The resulting solution was then diluted by thoroughly mixing it with 10% v/v nitric acid. Finally, the solution was analyzed using a Perkin Elmer/Sciex Elan 6000 ICP-MS. Quantification utilized a six-point calibration curve constructed with certified reference materials (CRMs: TDB-1, UMT-1, WGB-1, WMG-1, WPR-1) and in-house standards (LK NIP-1, NPD-1, OKUM-1, PJV-2)as detailed in Supplementary Table 5. All standards and samples monitored for peaks using two internal standards (^{115}In and ^{187}Re) through a drift monitor. The obtained results were corrected for interferences arising from nickel and copper. Procedural blanks and duplicates (1 per 10 samples) were included in each batch, with relative standard deviations (RSD) <10% for all elements. Certified reference material recoveries agreed with published values within ±15% (e.g., WPR-1 Au: certified 110 ± 11 ng/g vs. measured 123 ± 24.6 ng/g). The detection limits for analyses conducted at the Geoscience Laboratory are 0.01 ng/g for Ir, 0.08 ng/g for Ru, 0.02 ng/g for Rh, 0.17 ng/g for Pt, 0.12 ng/g for Pd, and 0.22 ng/g for Au.

Results

Sampling strategy and petrographical observations

In our investigation of the Kızıldağ ophiolite, we aimed to obtain a comprehensive suite of samples that represents a continuous ophiolitic section from the mantle to the extrusives. The sampling localities are illustrated in Figure 1. While the section along the road from Kale to Çevlik is generally considered continuous, Dilek and Delaloye (1992) identified normal faults in both the northern and southern regions of the ophiolitic massif. These normal faults have caused the gabbro and sheeted dikes, originally positioned above the stratigraphically shallower upper mantle, to now be situated above the deeper mantle peridotites (Fig. 1d). This displacement has resulted in the obscuration of the pre-obduction contact. Our sampling commenced at the mantle peridotites near Kale in the northwest, continuing systematically southeast along the road toward Çevlik, where we also collected samples from the gabbros and sheeted dikes. Despite the fault contact between the mantle peridotites and the overlying crustal section at both sites, our systematic sampling strategy allows us to assess the compositional variability of the mantle at varying depths. Furthermore, we collected numerous samples from various parts of the ophiolitic outcrops where possible, making our sampling more representative of the different depths of the mantle. This approach provides a comprehensive understanding of the geological context and the variability present throughout the ophiolitic section.

Mineral modal proportions were initially estimated through detailed optical microscopy. To validate these findings, a subset of samples was subjected to TIMA (Tescan Integrated Mineral Analyzer), and the resulting modal abundances were quantitatively compared to optical microscopy estimates. In the optical microscopy approach, it was assumed that all serpentine phases originated exclusively from olivine grains, and modal abundances were normalized to a total of 100%. The comparison between the optical microscopy and TIMA results demonstrated strong concordance, with discrepancies within approximately ±6–7% relative variance, highlighting the reliability of the micromethods employed.

The harzburgites of the Kızıldağ ophiolite are composed of olivine (56-86 vol.%), orthopyroxene (13-36 vol.%), and minor clinopyroxene (<5 vol.%) and chromian spinel (<2.3 vol.%; hereafter spinel) and characterized by mostly porphyroclastic textures (Fig. 2a, b).

Olivine porphyroclasts can reach maximum sizes of up to 2.5 mm and exhibit kink-band deformation. Orthopyroxene porphyroclasts, measuring up to 3-4 mm, exhibit pronounced elongation along cleavage planes and are occassionally enclosed by finer-grained, partly serpentinized olivine neoblasts (Fig. 2b). Certain harzburgite samples entirely lack clinopyroxene (Fig. 2c) or contain only trace amounts of primary clinopyroxene (Fig. 2d). Primary clinopyroxene was identified based on its relatively large grain size, subhedral to anhedral crystal habit, and its spatial occurrence enclosed between olivine and orthopyroxene or within residual textural domains, typically away from vein-like networks or interstitial areas. These grains also lack the wormy or interstitial morphology characteristic of secondary clinopyroxenes. Accessory spinel in these harzburgites typically occurs as anhedral to subhedral grains (Fig. 2e). However, some harzburgite samples exhibit enrichment in small, discrete clinopyroxene crystals, with sizes reaching up to 50×500 μm (Fig. 2f, g). These clinopyroxenes commonly display a worm-like morphology, occurring between olivine and orthopyroxene grains (Fig. 2h, j) or are found in association with spinel (Fig. 2k). The clinopyroxenes in these samples are interpreted to be predominantly secondary in origin, appearing to have crystallized from melt during percolation within the mantle. Additionally, clinopyroxene occurs along the edges of orthopyroxene grains, suggesting it may represent exsolution products of high-T orthopyroxene (Fig. 2f, g). However, the distribution of these clinopyroxenes does not appear to be solely the result of exsolution from high-T orthopyroxene, indicating that they may instead be crystallization products formed from percolating melt.

Based on petrographic features and whole-rock major and trace element compositions, the Kızıldağ harzburgite samples are subdivided into two groups, as detailed below and summarized in Table 1. The first group of samples (Group-1; 14 samples) predominantly lacks clinopyroxene. Although a few samples from this group contain small amounts of primary clinopyroxene, texturally observable secondary clinopyroxene is very rare and generally considered negligible (Fig. 2c-e). Clinopyroxene modal abundances in this group are less than 1.5 vol.%. Furthermore, two samples (K21 and K61) contain a few interstitial amphibole grains with sizes reaching up to 700 μm. The second group of samples (Group-2; 12 samples) exhibits abundant clinopyroxenes that are petrographically and chemically distinct from the rare, spatially isolated primary grains in Group-1. These clinopyroxenes are typically worm-like in appearance, fill the spaces between other phases, and occur along the margins of orthopyroxene grains (Fig. 2f-j), and are interpreted as secondary phases crystallized from percolating melts. The total modal abundances of clinopyroxene in Group-2 samples are higher than in Group-1, reaching up to 5.5 vol.%. Within this group, samples K16H, K26H, and K27H, located in close proximity to the gabbro and pyroxenite veins, contain a few very small plagioclase grains, reaching sizes up to 250 μm. These grains occur interstitialy among olivine and orthopyroxene crystals or embedded within the serpentinized matrix. Notably, their presence was detectable solely through BSE imaging (Fig. 2l). Additionally, samples K16H, K26H, K44, and K65 exhibit very minor interstitial amphibole grains, measuring less than 300 μm (Fig. 2i, l). Notably, the spatial distribution of Group-1 and Group-2 samples appears random throughout the field, lacking any distinct population clustering in specific locations (Fig. 1).

The ultramafic cumulates of the Kızıldağ ophiolite, representing the principal lithologies of the Moho transition zone (MTZ), consist of dunite and wehrlite. The cumulate dunite displays an adcumulate texture olivine (> 90 vol.%) that has undergone serpentinization along the rims. Wehrlite comprises moderately serpentinized olivine (55-60 vol.%) and clinopyroxene (35-45 vol.%). Above the MTZ, mafic cumulates include layered gabbroic rocks. Olivine gabbro contains olivine (10-35 vol.%, up to 3.5 mm) and clinopyroxene (35-40 vol.%, up to 5.5 mm), exhibiting subhedral to anhedral shapes. Olivine gabbronorite is characterized by olivine (10-20 vol.%, up to 4 mm), clinopyroxene (30-40 vol.%, up to 3 mm), and orthopyroxene (15-20 vol.%). Gabbro predominantly consists of plagioclase (35-45 vol.%, up to 2 mm) and minor clinopyroxene. The isotropic gabbroic rocks of the Kızıldağ ophiolite include gabbro, diorite, and quartz diorite, distinguished by their mineralogy and textures. Gabbro features granular to ophitic textures, with prismatic plagioclase (55-60 vol.%, up to 1.5 mm) and subhedral clinopyroxene (30 vol.%, up to 2 mm). Diorite is characterized by granular, ophitic to subophitic textures, comprising plagioclase (80 vol.%, up to 1.5 mm), hornblende (10-15 vol.%, up to 1 mm), and clinopyroxene (1-5 vol.%). Quartz diorite exhibits granular, ophitic, and micrographic textures, containing plagioclase laths (60-70 vol.%, up to 1.5 mm), hornblende (15-20 vol.%, up to 2 mm), clinopyroxene (5 vol.%, up to 1 mm), and quartz (10 vol.%). Sheeted dikes consist of diabase and quartz microdiorite, characterized by fine-grained chilled margins and medium-grained centers exhibiting subophitic and interstitial textures. Diabase exhibits intersertal and subophitic textures, comprising plagioclase (65-70 vol.%, up to 1 mm) and clinopyroxene (15-25 vol.%, up to 2 mm). The quartz microdiorite displays a microgranular porphyritic texture, with plagioclase (65-70 vol.%, up to 2 mm), hornblende (10-20 vol.%, <0.5 mm), and quartz (up to 10 vol.%, <0.18 mm). For a comprehensive examination of the petrographic characteristics of these crustal rocks and extrusives, readers are referred to Bağcı et al. (2005, 2008).

Whole-rock major and trace element geochemistry

The whole-rock major and trace element compositions for the mantle peridotite and crustal rock samples, as well as extrusives of the Kızıldağ ophiolite, are presented in Supplementary Table 1a. Mantle peridotites exhibit whole-rock Mg# values ranging from 89.4 to 92.2, and the contents of Al_2O_3, CaO, and Ti show negative covariations with MgO (Fig. 3). LOI values range from 4.4 to 16.5 wt.%.

Although there is some compositional overlap, Group-2 harzburgites generally exhibit higher concentrations of Al_2O_3 (0.56–2.55 wt.%), CaO (0.69–2.31 wt.%), and Ti (27–222 µg/g) compared to Group-1 harzburgites, which display Al_2O_3 contents ranging from 0.23 to 0.88 wt.%, CaO from 0.10 to 0.80 wt.%, and Ti from 6 to 44 µg/g. The Na_2O contents are low (below 0.02 wt.%) for both groups. Compared to the Oman peridotites depicted in Figure 3, the Kızıldağ mantle peridotites exhibit similar depletion trends in Al_2O_3, CaO, and Ti with increasing MgO content. While the majority of the dataset, particularly those from Monnier et al. (2006) align well with the Kıızldağ data, some data points from Kourim et al. (2022) and Hanghøj et al. (2010) exhibit slight Na enrichments that may result from localized effects of intense melt percolation. The chemical distinction between the two groups, together with petrographic evidence for secondary clinopyroxene growth, forms the basis for the subdivision between Group-1 and Group-2 harzburgites. All mantle peridotite samples show varying degrees of depletion relative to both the primitive mantle (PM) and the depleted MORB mantle (DMM), indicating their origins as residues from varying extents of melt extraction. Notably, Group-2 samples exhibit a lesser degree of depletion compared to PM and DMM, as evidenced by their elevated concentrations of Al, Ca, and Ti contents (Fig. 3).

The chondrite-normalized REE patterns and DMM-normalized multi-element variations for the mantle peridotites are illustrated in Figure 4a, b and e, f. Group-1 harzburgites exhibit a greater degree of depletion (Yb_N 0.09 to 0.14, Dy_N/Yb_N 0.15 to 0.37), displaying REE profiles that closely resemble the most depleted Oman peridotites. Group-2 harzburgites, in contrast, exhibit Yb_N values ranging from 0.17 to 0.70 and Dy_N/Yb_N values ranging from 0.30 to 0.76, and their REE patterns align well with those of the less depleted Oman peridotites.

Consequently, Group-1 harzburgites demonstrate progressive depletion from Lu to Gd, with nearly flat REE patterns or slight enrichment from Gd to La (Fig. 4a). Conversely, Group-2 samples show an almost flat or slightly depleted trend from heavy REE through middle REE, extending into the beginning of light REE (Nd). The REE patterns in Group-2 continue to appear nearly flat or exhibit slight enrichment from Nd to La (Fig. 4b).

Some samples from both groups of peridotites exhibit pronounced positive Pb anomalies, while all samples demonstrate positive Sr anomalies. With the exception of sample K45 from Group-2, which displays a negative Ti anomaly, both groups show slight positive Ti anomalies. The overall multi-element patterns reveal a depletion trend from heavy REE to middle REE and high field strength elements (HFSE), with this depletion being more pronounced in Group-1 samples. Additionally, an enrichment trend towards light REE and large ion lithophile elements (LILE) is observed (Fig. 4e, f).

Crustal rocks and extrusives exhibit whole-rock Mg# values ranging from 89.8 to 82.8 for ultramafic cumulates, 86.6 to 68.8 for mafic cumulates and isotropic gabbros, and 69.8 to 51.5 for sheeted dikes and basaltic extrusives. The contents of Al_2O_3, Na_2O, and Ti increase as MgO concentrations decrease from the lowermost crust to the uppermost crust, transitioning from ultramafic cumulates to mafic cumulates, isotropic gabbros, and ultimately to sheeted dikes and basaltic extrusives. Furthermore, while CaO exhibits a similar trend from ultramafic cumulates to isotropic gabbros, its concentrations begin to decline as MgO contents decrease from isotropic gabbros to sheeted dikes and basaltic extrusives (Fig. 3).

The ultramafic-mafic cumulates, isotropic gabbros, sheeted dikes, and basaltic extrusives exhibit chondrite-normalized REE patterns paralleling N-MORB, displaying varying degrees of depletion, which is particularly evident in the early formed ultramafic and mafic cumulates (Fig. 4c, d). Isotropic gabbros, sheeted dikes, and basaltic extrusives show enriched REE concentrations compared to mafic cumulates and closely align with N-MORB composition, although they display varying degrees of depletion (Fig. 4d). Across all crustal rock types and extrusives, the nearly flat REE pattern from Lu to Eu is disrupted by a slight depletion from Eu to Ce, which is particularly noticeable in mafic cumulates and isotropic gabbros. The pattern from Ce to La remains relatively flat in most samples, while it exhibits upward trends in others. Notably, one volcanic extrusive sample (K37A) displays a higher degree of depletion from Nd to La than other samples within the volcanic extrusive samples (Fig. 4d).

Ultramafic and mafic cumulates, as well as isotropic gabbros, exhibit broadly similar N-MORB normalized multi-element patterns, with ultramafic samples displaying greater depletion across all trace elements. Samples from these three groups are characterized by positive Sr anomalies, while some mafic cumulate samples show slightly more pronounced positive Eu anomalies (Fig. 4g, h). All three rock groups demonstrate an upward trend from Ce to Ba and Rb, indicative of enrichment in LILE. In contrast, the N-MORB normalized multi-element patterns of sheeted dikes and basaltic extrusives reflect similar trends but are more enriched than mafic cumulates and isotropic gabbros. Furthermore, most sheeted dikes and basaltic extrusives exhibit higher concentrations of REE and HFSE compared to boninites, displaying characteristics more akin to fore-arc basalts (Fig. 4h).

Mineral major element compositions

The electron microprobe results for spinel, olivine, orthopyroxene, clinopyroxene, amphibole, and plagioclase from the mantle peridotites and crustal rocks and extrusives are presented in Supplementary Table 2. Compositional variations of the average values from each sample are illustrated in Figure 5. Given the extensive serpentinization affecting many of the samples, microprobe analyses focused primarily on relict portions of silicate phases where available. In some highly serpentinized samples, alteration products, such as ferrian chromite or magnetite, were observed along the rims of spinel grains. However, these altered regions were clearly distinguishable from the primary spinel cores under BSE imaging. To minimize the effects of alteration, measurements of spinel composition always targeted the unaltered core of each grain.

Spinel in both groups of harzburgites displays a broad variation in Cr# [100×Cr/(Cr+Al)] and Mg# [$100\times Mg/(Mg+Fe^{2+})$] values, ranging from 46 to 70 and 43 to 76, respectively. These values exhibit a negative correlation. Compared to the Oman peridotites, the Kızıldağ spinels generally occupy the higher Cr# portion of the fore-arc field (Fig. 5a). In most Group-1 harzburgite samples, TiO_2 contents are typically low (<0.10 wt.%). However, certain samples, such as K14, K21, and K24, contain spinel that exhibits enriched TiO_2 levels ranging from 0.13 to 0.82 wt.%, with these samples showing variable distance to the MTZ, thereby representing various depths below MTZ. In Group-2 harzburgites, TiO_2 contents in spinel vary considerably, ranging from extremely low to 0.87 wt.%. Notably, spinel within the same sample may display significant TiO_2 variability. For example, the TiO_2 contents of spinel from sample K65 range from 0.16 to 0.72 wt.%. Despite this variability, a comparison of whole-rock LOI with spinel TiO_2 content reveals no significant correlation. For instance, sample K21 exhibits a low LOI value of 5.7 wt.% and a spinel TiO_2 content of 0.46 wt.%, while sample K14H shows a significantly higher LOI of 11.8 wt.% with a spinel TiO_2 of 0.40 wt.% (Supplementary Tables 1, 2). This further supports the conclusion that observed TiO_2 variations in spinel are primarily attributed to magmatic processes and subsequent metasomatism, with minimal influence from serpentinization. The Cr# values of spinel from Group-2 harzburgites shows a narrower range of 55 to 61, while Mg# values vary between 45 and 76. This range likely reflects both subsolidus re-equilibration, which modifies original magmatic compositions, and post-magmatic alteration (Su et al., 2021, 2023; Xiao et al., 2016). Data from both sample groups plot within the fore-arc field (Fig. 5a), indicating their close relationship to fore-arc mantle process. Spinel in both ultramafic and mafic cumulate samples exhibit variations in Cr# and Mg#, ranging from 39 to 73 and 25 to 67, respectively (Fig. 5a inset). The TiO_2 content in spinel displays a broad range, varying from 0.23 to 2.59 wt.%. The spinel in isotropic gabbro exhibits compositional variation similar to that observed in the spinel from ultramafic and mafic cumulates (Supplementary Table 2).

The olivine grains in all Kızıldağ harzburgite samples exhibit forsterite (Fo) contents ranging from 89.6 to 92.2, calculated as molar $Mg/(Mg+Fe^{2+})\times100$, plotting within the fore-arc peridotite field on the olivine-spinel mantle array diagram. Figure 5b reveals that olivine from the Kızıldağ peridotites has Fo contents similar to that of Oman peridotites, both exhibiting a highly refractory character. These high Fo and associated NiO (up to 0.5 wt.%) values were measured in large, kinked, relatively fresh olivine porphyroclasts, suggesting a highly refractory mantle source. Both Group-1 and Group-2 harzburgites display similar contents of NiO and MnO, with values ranging from 0.20 to 0.50 wt.% and 0.08 to 0.24 wt.%, respectively. The CaO content in olivine is consistently low (<0.08 wt.%) across most samples from both groups. A few small olivine neoblasts in some peridotite samples show elevated CaO contents, reaching up to 0.26 wt.%, even though the majority also exhibit low CaO content. The Fo content of olivine ranges from 79 to 89 in ultramafic cumulates and 74.1 to 86.8 in mafic cumulates (Fig. 5b inset). The NiO and MnO contents are less than 0.45 wt.% and range from 0.12 to 0.41 wt.%, respectively, while the CaO content consistently remains below 0.17 wt.% across all samples.

Orthopyroxene in harzburgite samples exhibits enstatite composition. The Mg# values from both groups fall within a similar range, varying from 90.4 to 92.2, and positively correlate with olivine Fo contents. The Kızıldağ orthopyroxenes show a similar range of Mg# values to the olivine as Oman peridotites, also reflecting the strong covariance of these phases (Fig. 5c). The Al_2O_3 and Cr_2O_3 contents range from 1.19 to 2.56 wt.% and 0.27 to 0.95 wt.%, respectively. The TiO_2 content in orthopyroxene from Group-1 harzburgites is less than 0.07 wt.%, while in Group-2 samples, it can reach up to 0.17 wt.%. Nearly all samples plot within the SSZ peridotite field (Fig. 5d), exhibiting TiO_2 enrichment levels similar to those observed in Oman samples. Orthopyroxene is present in both ultramafic and mafic cumulate samples, characterized by its enstatite composition and a wide Mg# range of 78.1 to 89.7. The Al_2O_3 and Cr_2O_3 contents vary from 0.96 to 2.74 wt.% and 0.10 to 0.89 wt.%, respectively, exhibiting positive covariation. The TiO_2 content is generally low but may reach up to 0.37 wt.% (Fig. 5d inset).

The classification of harzburgites into Group-1 and Group-2 is based on both petrographic characteristics and geochemical differences. Petrographically, Group-1 samples are distinguished by the absence or rarity of secondary clinopyroxene, while Group-2 samples contain abundant interstitial or wormy-textured secondary clinopyroxene. These textural features correlate with distinct geochemical patterns. Clinopyroxenes in both groups of harzburgites exhibit significant chemical heterogeneity, with Mg# values ranging from 91.8 to 96.3 in Group-1 (Wo: 40–50, En: 47–55, Fs: 2–5) and 92.1 to 94.0 in Group-2 (Wo: 36–49, En: 46–57, Fs: 3–7). Compared to orthopyroxene, clinopyroxene displays a weaker positive correlation with olivine Fo contents, similar to trends observed in Oman peridotites (Fig. 5e). Group-2 clinopyroxenes are generally more enriched in Al_2O_3 (1.61 to 4.07 wt.%) than those in Group-1 (0.23 to 3.07 wt.%.) Cr_2O_3 contents show comparable variations ranging from 0.22 to 1.45 wt.% for both groups. Clinopyroxene from Group-1 harzburgites is mostly depleted in TiO_2, with some grains contain up to 0.21 wt.% TiO_2. In contrast, the clinopyroxene from Group-2 samples is typically enriched in TiO_2, with concentrations reaching up to 0.51 wt.%, although some low TiO_2 grains are also present, mirroring trends observed in Oman peridotites (Fig. 5f). Clinopyroxene is present in all rock types forming the crustal section of the Kızıldağ ophiolite, with Mg# values decreasing from ultramafic cumulates (87-91) to volcanic rocks (74-84). TiO_2 content varies across the different rock types, reaching up to 0.86 wt.% in mafic cumulates and 0.81 wt.% in volcanic rocks (Fig. 5f inset). The Cr_2O_3 and Al_2O_3 contents in clinopyroxene range from 0.01 to 1.31 wt.% and 0.26-5.28 wt.%, respectively.

Plagioclase in mantle peridotite samples exhibits anorthite (An) contents, ranging from An_{89} to An_{91}, whereas plagioclase in mafic cumulates display a broader spectrum of An contents, varying from An_{88} to An_{99}. In contrast, the plagioclase found in isotropic gabbros shows significant alteration and generally exhibits much lower An contents, ranging from An_2 to An_{11}. Similarly, in sheeted dikes and volcanic rocks, plagioclase presents a diverse range of An contents from An_1 to An_{82}, with the low An values likely reflecting alteration processes (Supplementary Table 2).

Amphibole in mantle peridotites has pargasitic to tremolitic compositions (calcic group; Leake et al., 1997). These grains exhibit a high magnesium content, with Mg# values between 87 and 97. Additionally, there is considerable variability in the concentrations of Al_2O_3 (0.26–11.69 wt.%) and Cr_2O_3 (0.02–1.89 wt.%). While Na_2O concentrations are generally low, they can reach up to 1.88 wt.%, indicating a slightly higher abundance in some samples. TiO_2 shows a varying range, from low levels (0.02 wt.%) to higher concentrations (1.95 wt.%). Amphibole compositions within the crustal units of the Kızıldağ ophiolite demonstrate consistent variations across different rock types. Generally, TiO_2 content remains low in most amphiboles but can increase, reaching up to 4.48 wt.% in ultramafic cumulates, 1.31 wt.% in mafic cumulates, and up to 1.04 wt.% in isotropic gabbro and volcanic rocks samples. The Mg# values range from 76.5 to 95.2 in ultramafic cumulates, while amphiboles in other rock types exhibit Mg# values ranging from 50.3 to 95.7. The Al_2O_3 content shows wide-ranging variations, extending from 0.05 to 14.63 wt.%, while the Na_2O+K_2O content consistently remains below 3.21 wt.% in all amphiboles.

Clinopyroxene trace element compositions

The trace element compositions of clinopyroxenes, each representing analysis from different grain, analyzed from mantle peridotites and overlying ultramafic cumulates in the Kızıldağ ophiolite are listed in Supplementary Table 3. Within the Group-1 samples, clinopyroxenes with a primary texture from sample K72 exhibit an exceptionally ultra-depleted pattern from heavy REE to middle REE, followed by a subtle increase from Nd to La (Fig. 6a). Other primary clinopyroxenes from sample K74 demonstrate a slightly greater degree of heavy REE depletion; however, compared to the clinopyroxene from K72, they show significant enrichment in middle and light REE. Their REE profiles reveal a distinctive shift, transitioning from a relatively flat distribution of heavy to middle REE before gently declining from middle to light REE (Fig. 6a). Additionally, the clinopyroxenes from sample K76 display REE patterns very similar to those in K74, but with a slightly higher degree of light REE depletion. In the PM-normalized multi-element diagram, clinopyroxenes from sample K72 display positive anomalies for Ti and Hf, while a negative Ti anomaly is observed in sample K74 and K76. Clinopyroxenes from all three samples (K72, K74, and K76) display similar overall levels of LILE enrichment (Fig. 6b).

Most clinopyroxenes in Group-2 peridotites are secondary, occurring as interstitial grains. Some grains located at the edges of orthopyroxenes may represent exsolution products from high-T orthopyroxene. We analyzed interstial clinopyroxene, exluding exolution products, to constrain the composition of percolating melts. The heavy to middle REE compositions of secondary clinopyroxenes from Group-2 peridotites exhibit 3-4 times more enrichment compared to Group-1 samples, yet they remain depleted in light REE relative to DMM (Fig. 6c). Most secondary clinopyroxenes display Tm, Yb, and Lu concentrations below the abyssal peridotite field, while their middle REE (Dy to Sm) align with the abyssal peridotite field due to a positive slope from Lu to Dy. The REE patterns show a gentle decline from Dy to La (Fig. 6c). In the PM-normalized diagram, secondary clinopyroxenes from Group-2 samples exhibit negative anomalies for Ti, Zr, Sr, and Pb. Their LILE enrichment levels are comparable to those of Group-1 clinopyroxenes, although some grains show more pronounced enrichment (Fig. 6d). Contrastingly, a single grain from sample K66 in Group-2 exhibits REE pattern very similar to the primary clinopyroxene in sample K72 from Group-1, but with slightly more enriched light REE. It is characterized by ultra-depleted heavy REE to middle REE and a subtle decrease from Nd to La (Fig. 6c). The Ti anomaly in the multi-element graph is less pronounced compared to clinopyroxene in K72 (Fig. 6d).

Clinopyroxenes from the ultramafic cumulates display strikingly similar REE concentrations and chondrite-normalized REE patterns (Fig. 6d) as well as PM-normalized multi-element patterns (Fig. 6e) compared to those found in Group-2 mantle peridotites.

Orthopyroxene trace element compositions

The trace element compositions of orthopyroxenes from mantle peridotite samples are summarized in Supplementary Table 4. The orthopyroxenes in Group-1 and Group-2 mantle peridotites display comparable REE profiles; however, they exhibit significant inter-sample variability in Yb_N/Dy_N ratios, ranging from 1.5 to 26 (Fig. 7). This variability indicates that orthopyroxenes with higher Yb_N/Dy_N ratios experience a more pronounced depletion of middle REE relative to heavy REE (Fig. 7c, g), compared to their counterparts (Fig. 7a, e). While some orthopyroxenes exhibit homogeneous compositions in both their cores and rims, certain individual grains from other samples display varying levels of REE concentration, with significant enrichment in the rims relative to the cores (Supplementary Table 4). This results in lower Yb_N/Dy_N ratios, despite some core compositions demonstrating higher Yb_N/Dy_N ratios (Fig. 7g). In Figure 7, the most depleted orthopyroxene data from each sample, which represent the least metasomatized orthopyroxene, are indicated with purple symbols. Although heavy REE contents among orthopyroxenes from both groups show a relatively narrow range, Group-2 orthopyroxenes are distinctly enriched in light REE, resulting in a broader distribution relative to Group-1 orthopyroxenes. Despite an overall trend of depletion from heavy REE to middle and light REE across all orthopyroxene crystals, the effects of metasomatism lead to noticeable light REE enrichment in specific grains (Fig. 7).

In PM-normalized multi-element diagrams, orthopyroxenes with elevated heavy REE contents display only minor positive Ti anomalies, whereas those with lower heavy REE concentrations show more pronounced positive Ti anomalies. Furthermore, all orthopyroxenes exhibit positive Pb anomalies and significant enrichment of light REE and LILE relative to HFSE (Fig. 7).

Whole-rock HSE and Os isotope compositions

Supplementary Table 5 presents the concentrations of HSE and Os isotopic compositions of samples from the Kızıldağ ophiolite. Two harzburgite samples from Group-1, K14H and K24AH, exhibit depleted patterns in Pd, Re, and Au (Fig. 8a), corresponding to their low bulk Al compositions (Al_2O_3 = 0.23 wt.% and 0.62 wt.%, respectively). Sample K14H (spinel Cr# = 64) contains 3.5 ng/g Os, close to PM values, while the less depleted K24AH (Cr# = 55) has 1.112 ng/g Os. Sample K14H demonstrates a flat pattern from Os to Ru, followed by an inclination from Ru to Pd, and subsequently an increase from Pd to Re and Au. Sample K24H displays a zig-zag pattern with slight positive anomalies for Ir and Pt, although the overall trend from Os to Pt appears relatively flat. The negative trend from Pt to Pd continues upward through Pd to Re and Au (Fig. 8a). Sample K27AH from Group-2 possesses a slightly higher Os content (4.47 ng/g) than the PM and is characterized by an almost flat pattern from Os to Rh, exhibiting slight depletion compared to PM values. This pattern continues with a slight depletion from Rh to Pt, followed by increases from Pd to Re and further upwards to Au, ultimately surpassing PM values (Fig. 8a). The crustal rocks and extrusives, along with gabbro, pyroxenite, and rodingitized veins, exhibit a positive slope in their PM-normalized concentration levels from Os to Au, accompanied by notable depletion from Os to Rh in comparison to the mantle rocks. Their Pt, Pd, Re, and Au concentrations are comparable to those in mantle peridotites (Fig. 8b).

The $^{187}Os/^{188}Os$ ratios for Group-1 samples K14H (0.12475) and K24AH (0.12027) are lower than the primitive upper mantle estimate of 0.1296 (Meisel et al., 2001) and are associated with low $^{187}Re/^{188}Os$ ratios (<0.15). These unradiogenic Os isotope compositions reflect long-term Re depletion due to ancient melt extraction. In contrast, Group-2 sample K27AH, which contains the highest Al_2O_3 and CaO contents among the studied mantle peridotites (2.55 and

2.31 wt.%, respectively), has an even lower $^{187}Os/^{188}Os$ ratio (0.11795) but a moderately higher $^{187}Re/^{188}Os$ ratio of 0.27 (Fig. 8c). The elevated Re/Os in K27AH may indicate minor post-depletion metasomatism, yet its strongly unradiogenic Os signature still preserves evidence of ancient depletion. Re-depletion ages (T_{RD}) for both groups range between 0.7 and 1.6 Ga, indicating Proterozoic melt extraction events (Supplementarty Table 5). The calculated TRD ages suggests that these peridotites originated from a mantle domain that experienced major melt depletion in the Proterozoic, with Group-2's higher Re/Os reflecting localized late-stage modification without resetting the Os isotope system. Ultramafic to mafic cumulate and sheeted dike samples exhibit $^{187}Os/^{188}Os$ ratios ranging from 0.13221 to 0.21804, with $^{187}Re/^{188}Os$ ratios varying from 2.45 to 46.4. One basalt sample shows a notably high $^{187}Os/^{188}Os$ ratio of 0.28326 and an $^{187}Re/^{188}Os$ ratio of 107.2. The plagiogranite in the Kızıldağ ophiolite, situated at the upper part of the sheeted dikes, has a $^{187}Os/^{188}Os$ ratio of 0.22780 and a $^{187}Re/^{188}Os$ ratio of 47.3. Additionally, the pyroxenite, gabbro, and rodingite veins in the mantle harzburgites have $^{187}Os/^{188}Os$ ratios of 0.13351 to 0.18010 and $^{187}Re/^{188}Os$ of 6.55 to 49.7. All analyzed samples scatter along the 94 Ma reference line, although some exhibit higher $^{187}Os/^{188}Os$ or lower $^{187}Re/^{188}Os$ ratios compared to this reference line. However, both rodingite vein and basalt sample show higher $^{187}Re/^{188}Os$ ratios than the reference line (Fig. 8c).

Discussion

Effects of serpentinization on compositions of mantle peridotites

The mantle peridotites of the Kızıldağ ophiolite have undergone metamorphism, resulting in the formation of serpentinized peridotites. Although serpentinization has minimal impact on the major elemental composition of mantle peridotites, calcium emerges as the only element influenced, albeit to a limited degree (Palandri et al., 2004). This serpentinization process contributes to an increase in water content and enhances the concentrations of fluid-mobile elements (FME) such as Sr, Pb, Ba, and U, which are influenced by various physicochemical conditions and rock-fluid interactions (Guillot et al., 2013; Wu et al., 2020). In our samples, LOI values range from 4.4 to 15.65 wt.%, indicating varying degrees of post-magmatic alteration. However, geochemical analyses demonstrate that the concentrations of major and trace elements, including FME, do not exhibit significant correlations with LOI values (Supplementary Table 1b). This lack of correlation implies that the observed elemental concentrations primarily reflect mantle processes with minimal serpentinization effect.

While the major and trace element data suggest a limited influence of serpentinization, the behavior of HSE and Os isotopes requires further scrutiny. The Re-Os isotopic system is often considered relatively robust due to Os's affinity for alteration-resistant sulfides (Shirey and Walker, 1998; Brandon et al., 1999), potentially preserving primary mantle signatures. However, fluid-mediated HSE mobilization, particularly Re, is still possible during serpentinization. Given the limited dataset (n=3) from Kızıldağ peridotites, the possible correlations between LOI and $^{187}Os/^{188}Os$, $^{187}Re/^{188}Os$ ratios, and some HSE (Pd, Re, Au) must be interpreted with extreme caution (Supplementary Table 1b). The tight clustering of two data points, with the third exerting disproportionate influence on any linear trend, suggests that these correlations might be spurious and not representative of a true relationship. Therefore, interpretations regarding serpentinization's impact on the HSE and Os-isotope system in the Kızıldağ ophiolite demand extreme caution, considering the small sample size, the distinct geochemical properties of the HSE, and the undue influence of the single, more divergent data point.

Temperature, pressure, and oxygen fugacity conditions

The temperature, pressure, and oxygen fugacity (fO_2) conditions of mantle peridotites provide critical insights into their formation and geodynamic evolution. We calculated temperatures using the Ca-in-orthopyroxene thermometer (Brey and Köhler, 1990), pressures via the Al-in-orthopyroxene barometer (Mercier, 1980), and fO_2 following Ballhaus et al. (1991). The two-pyroxene thermometer was excluded due to the prevalence of secondary clinopyroxene, which likely formed through metasomatic melt interactions and is not in equilibrium with orthopyroxene. This disequilibrium is evident in clinopyroxene Mg# values, which deviate significantly from the 1:1 trend defined by coexisting olivine Fo content (Fig. 5e). In contrast, orthopyroxene Mg# and olivine Fo align closely along the equilibrium line (Fig. 5c), validating the use of Ca-in-orthopyroxene thermometry.

To further test the equilibrium between orthopyroxene and clinopyroxene in the Kızıldağ mantle peridotites, we employed the approach of Agranier and Lee (2007), which assesses REE partitioning by plotting Opx/Cpx ratios against the cation radius of trivalent REE (Fig. 9a). Under equilibrium conditions, these ratios exhibit a smooth, concave-downward trend from heavy to light REE, consistent with theoritical partitioning curves at temperatures between 1000 and 1400 °C. However, most Kızıldağ samples deviate significantly from equilibrium, displaying distinct concave-upward (U-shaped) REE profiles indicative of significant disequilibrium. This disequilibrium is particularly pronounced in Group-2 samples (K65, K66, K68), where seconday clinopyroxene formed from melts percolating through the peridotite. Group-1 samples exhibit varying degrees of deviation; samples K72 and K74 approaches equilibrium, whereas K76 shows a pattern similar to the disequilibrated Group-2 samples.

To minimize the effects of secondary overprinting, we used orthopyroxene core compositions, excluding REE-enriched rims associated with metasomatism. For clinopyroxene, limited grain sizes necessitated single-point analyses; nonetheless, the relatively homogeneous REE profiles within individual grains allowed us to select the most depleted clinopyroxene compositions as representatives of the least metasomatized components. Disequilibrium is characterized by distinct REE fractionation patterns: compared to Group-1 peridotites, Group-2 samples display lower Opx/Cpx ratios in the heavy REE region due to higher concentrations of heavy REE in secondary clinopyroxenes formed from melt percolation. Conversely, ratios are elevated in the light REE region. This contrasting behavior signifies differential REE retention: orthopyroxene cores preserve the primary melting signature with minimal seconday influence, whereas the secondary clinopyroxenes, enriched in heavy REE, likely crystallized from more fertile melts derived from the asthenospheric mantle. The depletion of light REE in these clinopyroxenes reflect their low partition coefficients, while orthopyroxenes preferentially incorporate light REE due to slower diffusion or boundary exchange process, resulting in anomalous light REE enrichment relative to secondary clinopyroxene.

The near-equilibrium signatures observed in some Group-1 peridotites (e.g., K72, K74), characterized by scarce or absent secondary clinopyroxene, suggests either partial equilibration at elevated temperatures or limited late-stage melt influence. In contrast, the pronounced concave-up REE patterns in Group-2 peridotites (e.g., K65, K66, K68), reflect metasomatic overprinting, evidenced by secondary clinopyroxene formation and REE distribution within orthopyroxene. Collectively, these observations suggest a complex melting and metasomatic history, with orthopyroxene-clinopyroxene REE disequilibrium serving as geochemical fingerprint of melt–rock interaction that persisted through ascent and cooling process.

Group-1 samples yield pressures of 1.6–2.3 GPa and temperatures of 1087–1349 °C, while Group-2 samples span 1.5–2.4 GPa and 1081–1386 °C (Supplementary Table 6), sharing overlapping P-T ranges which reflect dynamic processes during subduction initiation. While Oman samples exhibit a wide range of thermal states extending to pressures as high as 3 GPa (excluding some anomalously high P and T, which might be potentially linked to deep melting or metasomatic resetting), the Kızıldağ data align more closely with the higher pressure and temperature portion of the Oman distribution, lacking the lower pressure and temperature samples observed in Oman (Fig. 9b). While some melting may have initiated in the garnet stability field, the Kızıldağ data cluster predominantly within pressures below 2.5 GPa, indicating a polybaric melting history with additional melt production occurring at shallower levels during subduction initiation. The presence of clinopyroxene-spinel association in some samples and the trace element signatures of orthopyroxene with Yb_N/Dy_N ratios ranging from 1 to 26 support the high-pressure conditions observed, indicating a transition from initial high-temperature melting that extended from the garnet to spinel stability fields. Furthermore, several Kızıldağ samples exhibit higher temperatures at given pressures or, conversely, lower pressures at equivalent temperatures compared to Oman, indicative of rapid decompression following deep melting events. These high-T signatures may suggest relatively fast ascent, which limited thermal re-equilibration at shallower levels.

Further analysis focused on calculating oxygen fugacity conditions for the peridotites, utilizing the equation proposed by Ballhaus et al. (1991). The results revealed a range of ΔfO_2 from -2.14 to 0.27 (FMQ), with one sample reaching 2.00, and an average value of -0.28 for Group-1 samples. In contrast, Group-2 samples exhibited ΔfO_2 values ranging from -0.59 to 1.24, with an average of 0.39 (Supplementary Table 6). The relatively higher oxygen fugacity values observed in Group-2 highlight the more hydrous nature of the mantle wedge from which these samples originated. This enhanced hydrous character likely contributed to a greater amount of melt interacting with the overlying mantle, as evidenced by the increased abundance of secondary clinopyroxene in Group-2 samples. These clinopyroxene crystals are likely crystallized from the metasomatizing melt during the percolation process within the mantle wedge.

Ultimately, the combined P–T, fO_2, geochemical, and mineralogical evidence suggests that the Kızıldağ mantle wedge experienced a transient, high-temperature regime associated with relatively fast ascent during subduction initiation and subsequent fluid-mediated mmetasomatism. This thermal regime precludes extensive re-equilibration, preserving high-temperature signatures that record early subduction processes.

Nature and effects of multiple metasomatizing agents on mantle peridotites

Figure 10a illustrates the correlation between whole-rock Y content and the Cr# of spinel crystals for both Group-1 and Group-2 mantle peridotites. Group-1 samples demonstrate consistently low Y content, regardless of inreasing spinel Cr# values. In contrast, the Group-2 samples, which exhibit spinel Cr# values ranging from 50 to 60, show varying degrees of Y enrichment. This trend aligns with the presence of secondary clinopyroxene and amphibole in Group-2 samples, as well as elevated whole-rock Al and Ca contents (Fig. 3) and enriched REE compositions compared to Group-1 samples (Fig. 4), indicating their susceptibility to modal metasomatism. When compared to the Oman peridotites, the Kızıldağ samples display significantly higher Y, which may indicate a different degree of melt addition in that tectonic setting. Nonetheless, the diagram does not clarify the specific nature of the melt interactions experienced by the mantle peridotites.

Previous studies have provided compelling evidence supporting the SSZ origin of the Kızıldağ ophiolite, with interpretations based on observations of cumulate rocks (Bağcı et al., 2005) and mantle peridotites (Uysal et al., 2012a; Chen et al., 2019; Aldanmaz et al., 2020; Lin et al., 2020;). In this study, the detailed examination of whole-rock trace element compositions and mineral chemistry data from both the mantle and crustal sections of the ophiolite corroborate the SSZ origin of the ophiolite. Notably, the depleted heavy REE patterns (Fig. 4), along with the relatively high spinel Cr# of the non-metasomatized (or least metasomatized) mantle peridotites (Fig. 5), suggest an SSZ origin. Furthermore, mineral compositions and N-MORB-like multi-element patterns of the crustal rocks and extrusives, exhibiting HFSE depletion and LILE enrichment (Fig. 4c-h), indicate their crystallization from SSZ-type melts. The multi-element patterns of the ultramafic cumulates fall within the fields characteristic of fore-arc basalts to boninites, reinforcing the subduction-related origins of these rocks.

The subduction initiation model proposed by Reagan et al. (2019, 2023) involves a series of complex and dynamic processes driven by lithospheric extension, mantle upwelling, and the onset of subduction-related magmatism. Central to this model is the concept of spontaneous lithospheric foundering, wherein buoyant lithospheric material undergoes gravitational instability and sinks into the asthenosphere. This process is driven by lithospheric thinning and weakening due to extensional tectonic forces, creating zones of lithospheric vulnerability that are prone to foundering (e.g., Gurnis et al., 2004; Gerya, 2011). As lithospheric foundering progresses, mantle upwelling occurs beneath the thinned lithosphere, triggering decompression melting and generation of basaltic magmas. These tholeiitic magmas, known as fore-arc basalts, are erupted onto the overriding plate, marking the onset of subduction-related volcanism. In addition to fore-arc basalts, the subduction initiation model also recognizes the formation of boninites, a distinct type of volcanic rock associated with subduction initiation environments. Boninites are characterized by high Mg and Si contents, elevated concentrations of incompatible trace elements, and lower Ti content compared to fore-arc basalts. They are believed to originate from highly depleted mantle sources undergoing partial melting in response to the rapid influx of fluids released during the early stages of subduction initiation (e.g., Stern et al., 2012; Pan et al., 2024). Consequently, the percolation of distinct types of melts into the overlying mantle significantly influences its compositional variability (Zhang et al., 2024).

Figure 10b illustrates the relationship between spinel TiO_2 and whole-rock Y content for Group-1 and Group-2 peridotites. In this diagram, whole-rock Y content serves as an indicator of modal metasomatism, while spinel TiO_2 content reflects the influence of melts with varying Ti contents on spinel crystals. In the Group-1 samples, a significant proportion resides within the low whole-rock Y and low spinel TiO_2 field (area G1a; Group-1a), suggesting a lack of (or negligible) modal metasomatism and minimal interaction with TiO_2-enriched melts or TiO_2-poor melts. However, a subset of Group-1 samples exhibits increased spinel TiO_2 contents relative to their low Y contents (Line G1b; Group-1b), indicating various degrees of interaction with TiO_2-enriched melts in the absence of significant modal metasomatism. Conversely, samples along Line G2a (Group-2a), while displaying varying degrees of Y enrichment, lack significant TiO_2 enrichment in spinel crystals. This implies interaction with TiO_2-depleted melts and concurrent modal metasomatism. Similarly, the remaining Group-2 samples, following Line G2b (Group-2b), demonstrate elevated Y contents alongside increased spinel TiO_2 contents, suggestingconcurrent interaction with partially TiO_2-enriched melts and modal metasomatism. When compared to the Kızıldağ data, the Omani samples appear to show similarly Ti and Y enrichment trend.

To gain deeper insights into the nature of melts interacting with mantle peridotites, Figure 10c compares the Cr# values of spinel crystals with their TiO_2 contents. The melt extraction process, resulting from asthenospheric upwelling due to decompression during the initial stages of subduction, leads to the formation of a depleted lithospheric mantle characterized by spinel with elevated Cr# and depleted TiO_2 contents (Müntener et al., 2006; Jean et al., 2010). Consequently, spinel crystals within the fore-arc mantle that interact with Ti-poor boninitic melts do not exhibit significant enrichment in TiO_2. However, this interaction leads to a notable increase in spinel Cr# values following melting. Conversely, when spinel crystals engage with Ti-rich arc tholeiites or MORB-like melts, a parallel increase in TiO_2 concentrations is observed along with elevated spinel Cr# values (Arai, 1994). In Figure 10c, Group-1a and Group-2a mantle peridotites from the Kızıldağ ophiolite predominantly align along the peridotite-boninitic melt interaction trend. In contrast, samples from Group-1b and Group-2b display a distribution following the compositional variation toward the Izu-Bonin-Mariana island arc tholeiite composition and along the peridotite-IAT interaction trend. Although similar TiO_2 enrichments are observed in Oman peridotites, the Oman dataset additionally records evidence of MORB-like melt interaction, a feature absent in Kızıldağ samples. This diagram indicates that interaction with IAT and boninitic melts has resulted in differential TiO_2 enrichment of spinel composition within mantle peridotites, concurrently leading to secondary mineral crystallization and, thus, modal metasomatism in select samples during melt interaction.

As depicted in Figure 10d, clinopyroxene crystals with the highest TiO_2 contents in each sample from Group-1b and Group-2b exhibit similar TiO_2 enrichment trends to those observed in the spinel crystals from these samples. This observation suggests that while primary clinopyroxenes undergo partial Ti enrichment during melt interaction, secondary clinopyroxene crystallization begins from these melts. Notably, secondary clinopyroxenes from Group-2b samples, influenced by modal metasomatism, display significant Ti enrichment. Similar Ti enrichment is also observed in some orthopyroxenes from both Group-1 and Group-2 samples, particularly in samples interactions with IAT-like melts (Fig. 10e). Both clinopyroxene and orthopyroxene from the Kızıldağ samples exhibit more pronounced Ti enrichment, indicative of a stronger metasomatic overprint, compared to Oman samples.

Mineral and whole-rock insights into partial melting and cryptic/modal metasomatism

Modal mineralogy is commonly used as an indicator of depletion in mantle peridotites, with clinopyroxene typically being more rapidly depleted than other mantle minerals during partial melting. As such, highly depleted mantle peridotites may exhibit either scarcity or the preservation of very rare primary clinopyroxene. However, trace element compositions of clinopyroxene and orthopyroxene, as well as the Al content of spinel, provide valuable insights into the degree of melting (Arai, 1994; Sano and Kimura, 2007; Scott et al., 2016). Nonetheless, the whole-rock composition of mantle peridotites may not always directly reflect the true extent of partial melting, especially in the case of modal metasomatized samples. Whole-rock major and trace element compositions, along with spinel and olivine mineral compositions from the Kızıldağ mantle peridotites, indicate that these samples are residues of mantle material following varying degrees of partial melting. To assess the melting processes, we employed forward modelling based on (1) whole-rock major and trace element compositions, (2) major element composition of spinel, and (3) trace element abundances in clinopyroxene and orthopyroxene.

Whole-rock geochemical insights

It is essential to note that previous sections have emphasized the effects of metasomatism through melt impregnation in these mantle peridotites. The introduction of secondary clinopyroxene as well as rare amphibole in some samples, which acts as the primary carrier of heavy REE-during melt percolation, has led to an enrichment of bulk REE contents. This suggests that the whole-rock REE compositions of many samples may not accurately reflect the true degree of melting. Consequently, whole-rock modelling, particularly for metasomatized samples, yields lower estimates of partial melting compared to those derived from spinel compositions. However, the whole-rock compositions of the least metasomatized Group-1 samples may provide a more accurate assessment of melting degrees.

In the Kızıldağ ophiolite, the Al_2O_3 and CaO contents of mantle peridotites range from 0.23 to 2.55 wt.% and 0.10 to 2.31 wt.%, respectively, suggesting varying degrees of depletion. Figure 3 illustrates that Group-2 samples exhibit a less depleted signature compared to Group-1 samples. In the chondrite-normalized REE diagram (Fig. 4), Group-1 peridotite samples indicate 18-20% melting, whereas Group-2 peridotite samples show less depletion, with samples plotting along non-modal fractional melting curves representing 10-17% melting. However, as previously discussed, petrographic observations indicate that the Group-2 mantle peridotites show signs of modal metasomatism, with clinopyroxene in these samples not reflecting their primary origin but rather representing crystallization products of melts percolating through the overlying mantle (Fig. 3e-j). Consequently, the whole-rock composition of modal metasomatized Group-2 samples may not accurately portray the original degree of depletion experienced by the mantle.

Constraints from spinel compositions

Spinel serves as a robust indicator in mantle petrology, with its Cr# providing a quantitative measure of melting. This is supported by the positive correlation between Cr# values in spinel and the extent of melting (Hellebrand et al., 2001). Although complex metasomatic and metamorphic processes may obscure the primary residual origin of mantle materials, spinel is generally considered as a more reliable indicator than silicate phases, which are more susceptible to alteration by metasomatism. The spinel grains in the Kızıldağ mantle peridotites exhibit moderate to high Cr# values, ranging from 46 to 70. This suggests that the peridotites analyzed in this study represent residues of a higher degree of melt extraction compared to abyssal peridotites, where spinel Cr# values below 60. Applying the equation proposed by Hellebrand et al. (2001) [$F = 10\times\ln(Cr\#) + 24$] to the analyzed spinels from both groups indicates a melting degree of 17-20% (Supplementary Table 2), which is consistent with the melting degree inferred from whole-rock heavy REE contents for Group-1 samples (Fig. 4a). The high Cr# values of spinels (up to 75) and elevated Fo contents in olivines (up to Fo 92.2) observed in the Kızıldağ peridotites are indicative of extensive melt depletion under hydrous conditions. Experimental studies show that under anhydrous conditions, spinel disappears at Cr# values significantly lower than those recorded here, suggesting that hydrous flux melting was necessary to stabilize spinel at such high Cr# (e.g., Jaques and Green, 1980; Barret et al., 2022). This hydrous melting scenario, consistent with subduction initiation environments, also explains the extreme refractory character of the peridotites.

Melting modelling from trace element composition of clinopyroxene

Similar to spinel, the REE compositions of clinopyroxene provide valuable insights into the degree of melting of mantle peridotites, as REE exhibit the highest partition coefficients in clinopyroxenes within spinel peridotites. However, their compositions may also reflect the influence of metasomatic processes (e.g., Rivalenti et al., 1996). Aldanmaz et al. (2020) reported the major and trace element compositions of mantle phases from the Kızıldağ ophiolite, suggesting that these peridotites experienced more than 16% melting. They noted that many clinopyroxene grains in these samples exhibit lower absolute concentrations of heavy REE compared to the typical range observed in abyssal peridotites, proposing that these grains may record higher degree of melt extraction than those formed in a MOR environment. In the Kızıldağ ophiolite, most clinopyroxenes are secondary, occuring as small blebs interstitially along grain boundaries, and occasionally penetrating existing mantle minerals. The REE patterns of most clinopyroxenes plotted in Figure 6a of Aldanmaz et al. (2020) indicate that their heavy REE concentrations fall between the melting curves for 6 and 13% melting, considerably lower than the melting estimates they reported based on spinel composition. The REE patterns of these clinopyroxenes closely resemble those of secondary clinopyroxenes from our Group-2 samples, as well as clinopyroxenes from the ultramafic cumulates reported in our study (Fig. 6). However, some of the studied clinopyroxenes display slightly elevated heavy REE concentrations compared to those in Aldanmaz et al. (2020). Notably, a few clinopyroxene grains analyzed by Aldanmaz et al. (2020) closely resemble the primary clinopyroxenes identified in our Group-1 samples. Although the number of samples from which the clinopyroxene trace element composition was obtained in our study is limited, we observed that some clinopyroxenes suggest that melting initiated in the garnet stability field and continued into the spinel stability field, rather than occurring solely within the spinel facies.

The trace element compositions of primary clinopyroxenes from two peridotite samples of Group-1 indicates approximately 17-23% melting. Clinopyroxenes from sample K72 exhibit a rapid depletion of middle REE relative to heavy REE (Fig. 6a), which can be modelled as an initial ~15% melting in the garnet stability field, followed by approximately 8% melting in the spinel stability field. Conversely, the heavy REE compositions of clinopyroxenes from sample K74 suggest 17-18% melting in the spinel stability field, with notable enrichment of middle to light REE attributed to metasomatic processes (Fig. 6a). In contrast, clinopyroxenes from other samples, particularly those in Group-2, display enriched REE compositions and are of secondary origin, as indicated by petrographic observations of their small size and characteristics typical of crystallization from percolating melts. Their REE and multi-element variations closely resemble those of clinopyroxene found in ultramafic cumulates. Consequently, these clinopyroxenes are unsuitable for constraining melt depletion signatures. Although the trace element concentrations within primary clinopyroxenes can provide valuable insights into both the degree of partial melting and the influence of metasomatic agents, the modal abundances of primary clinopyroxene significantly decrease when mantle melting exceeds 20%. This depletion leads to the formation of an orthopyroxene-olivine-spinel residue (Walter, 2003), thereby positioning orthopyroxene as the primary carrier of trace elements. The limited occurrence and reduced grain sizes of residual clinopyroxene may hinder accurate characterization of melting processes. The small sizes of these clinopyroxene grains increase their vulnerability to alteration by metasomatic agents, allowing these agents to affect even the cores of the clinopyroxene crystals, not just the rims. This may result in compositions reflecting metasomatic alteration rather than a true representation of the degree of melting.

Inferring partial melting and metasomatism through orthopyroxene trace element analyses

One of the challenges in geochemical modelling of partial melting events in mantle peridotites is defining the trace element and mineralogical composition of the starting material. In this study, we assume that mantle processes associated with subduction initiation have influenced the Kızıldağ mantle peridotites, similar to other Tethyan mantle peridotites. In this context, the asthenospheric mantle rises and begins to melt during subduction initiation. Accordingly, we employed the trace element composition of the depleted MORB mantle (DMM; Salters and Stracke, 2004) as the initial point (C_0; Supplementary Table 7). The mineralogical composition of the DMM may vary betweengarnet- and spinel-bearing mantle assemblages, depending on the depth of partial melting during ascent. For instance, we first examined the effects of both garnet- and spinel-facies partial melting models on one orthopyroxene composition from the Kızıldağ samples (sample K65; Fig. 11). The mineral and melt modes for spinel and garnet lherzolite are as follows: $\mathrm{Ol}_{0.55(-0.22)}$ + $\mathrm{Opx}_{0.25(0.38)}$ + $\mathrm{Cpx}_{0.18(0.71)}$ + $\mathrm{Sp}_{0.02(0.13)}$ and $\mathrm{Ol}_{0.55(0.08)}$ + $\mathrm{Opx}_{0.20(-0.19)}$ + $\mathrm{Cpx}_{0.15(0.81)}$ + $\mathrm{Gt}_{0.10(0.30)}$, respectively (Sano and Kimura, 2007), where the numbers in parentheses indicate the melt mode.

In the open-system melting models, the mass flux rate (β) is defined as the influx mass fraction (relative to the initial solid) divided by the degree of melting (Ozawa and Shimizu, 1995). The observed variability in light REE abundances within the residual compositions can be reproduced by modulating the mass flux rate. For simplicity, the critical melt porosity (Φ) was set to 0, which reduces the equation to a straightforward fractional melting model. The partition coefficients (*Kd*) utilized in our models are sourced from Sano and Kimura (2007) (Supplementary Table 6).

In the next step, we modelled the enriched REE abundances of the orthopyroxenes obtained from the rims of the minerals. The composition of basaltic melt (C_B; Supplementary Table 7) was derived from 6% partial melting of a hypothetical depleted-DMM source ($C_{D\text{-}DMM}$; Supplementary Table 7), which is calculated based on 18% melt extraction (15% in garnet-facies melting and 3% in spinel-facies melting) from the DMM composition.

As illustrated in Figure 11a, the REE abundances of orthopyroxenes from sample K65, modelled in equilibrium with residues after 5% to 10% melt extraction in the spinel stability field, exhibit semi-parallel trends from heavy REE to middle REE. However, the REE abundances observed in orthopyroxene from sample K65A demonstrate a more pronounced depletion in middle REE compared to the modelled compositions for 5% and 10% depletion. This suggests that the Kızıldağ mantle peridotites are unlikely to have undergone partial melting within the spinel stability field, a conclusion supported by the clinopyroxene REE composition of sample K72 from the Group-1 samples. Similarly, applying the same models using garnet lherzolite assemblages produced results that did not align with the REE abundances of sample K65 (Fig. 11b). These findings further indicate that the Kızıldağ mantle peridotites are not residues from partial melting within the garnet stability field, also supported by petrographic observations revealing a significant presence of spinel.

Building on these models and considering recent evidence that many global mantle peridotites experience melting first in garnet and subsequently in spinel facies (e.g., Hellebrand et al., 2002; Gong et al., 2016, 2020), we propose a two-stage melting model for the Kızıldağ mantle peridotites. In this model, the DMM underwent depletion in garnet facies during the first stage, followed by spinel facies in the second stage. The reaction governing the garnet-to-spinel breakdown, which involves the consumption of olivine and garnet to produce orthopyroxene, clinopyroxene, and spinel, is derived from Johnson et al. (1990). To obtain more representative results for light REE abundances, we applied the open-system dynamic melting equation proposed by Ozawa and Shimizu (1995). Given that the Kızıldağ mantle peridotites formed in a supra-subduction zone context, we included the subduction zone component (Eiler et al., 2000, 2007) ashe fluxing material that is incorporated into the residual composition during the melting process (i.e., wet melting).

The outcomes of the open-system fractional melting models for orthopyroxene from the Kızıldağ mantle peridotites are summarized in Figure 12. A critical observation is the variable and parallel REE (particularly heavy REE) abundances across most samples, a characteristic that a single melting model cannot adequately explain. This variation suggests that the orthopyroxenes may have undergone either (a) differing degrees of melting or (b) enrichment during subsequent melt interactions following depletion. It is important to note that the higher REE compositions have been obtained from the rims of the orthopyroxenes, which precludes variable depletion by different degrees of melting. In either scenario, the lowest REE abundances documented in the orthopyroxenes from each sample provide the most reliable estimates of depletion due to partial melting.

To reproduce the lowest REE abundances obtained from each sample in the initial modelling step, we constructed multiple models that examined varying degrees of melting (F) within the garnet and spinel stability fields. The models operating in the garnet stability field were assumed to occur under dry conditions (β=0), where β represents the activity of free water in the system. In contrast, the models within the spinel stability field were considered open systems with variable values for β. As depicted in Figure 12, the lowest REE abundances observed in most orthopyroxene compositions can be effectively reproduced through these two-stage melting events. The results summarized in Table 1 reveal that the lowest REE abundances of the orthopyroxenes can be explained by 5-17% melting in the garnet-stability field, followed by 4-10% melting in the spinel stability field. Total melting degrees reach up to 24.5%, which results in the consumption of primary modal clinopyroxene. It is worth noting that the observed low degrees of melting (e.g., 13% for sample K16H) may be due to the analysed point being close to the rim, indicating metasomatic effects, or the complete modification of the orthopyroxene by REE-rich metasomatizing agents, facilitated by its smaller size, which allowed for full equilibration.

These results highlight the complexity of melt generation and modification processes in the Kızıldağ mantle peridotites. Our findings suggest that the two-stage melting model, which incorporates both dry conditions in the garnet stability field and open-system behaviour in the spinel stability field, offers a robust framework for understanding the geochemical evolution of these peridotites. The concentrations of Ti and Yb in orthopyroxene are expected to show a positive correlation, with Ti depleting more rapidly than Yb during melting due to its higher incompatibility (Fig. 10e). Given the moderately to highly depleted characteristics of the Kızıldağ mantle peridotite, as indicated by spinel Cr# and orthopyroxene trace element concentrations as well as the lack of primary clinopyronene in most samples, orthopyroxenes in these samples are expected to exhibit markedly low Ti concentrations. Most orthopyroxenes from both Group-1a and Group-2a samples correspond to the most depleted segment of the diagram, characterized by minimal concentrations of Yb and Ti, suggesting limited influence from metasomatism (Fig. 10e). In contrast, Group-1b orthopyroxenes demonstrate a slight enrichment of Ti compared to those from Groups-1a and -2a, while maintaining comparable Yb contents. Notably, one data point within this group exhibits extreme enrichment in Ti alongside slight enrichment in Yb. While most orthopyroxenes from Groups-1a and -2a display similar Ti levels, certain rim compositions of orthopyroxene grains from Group-2b reveal elevated Ti and Yb concentrations compared to their lower Ti counterparts. The consistently low Yb concentrations across nearly all orthopyroxenes suggest a high degree of depletion (Fig. 10e). Given that orthopyroxene is predominantly in equilibrium with clinopyroxene, the elevated Ti levels imply that Ti was introduced to the peridotites via metasomatic processes. Consequently, the data support the conclusion that certain Kızıldağ peridotite samples experienced enrichment from a light REE- and Ti-bearing metasomatic agent (e.g., island arc tholeiite melts), while the remaining samples reflect modification by a light REE-rich but Ti-poor metasomatic source (e.g., boninitic melts or slab-derived fluids). Although carbonatite metasomatism could theoretically produce Ti-poor, light REE-rich signatures, the absence of extreme light REE enrichment or carbonate mineral assemblages in these samples favors a subduction-related origin for both metasomatic endmembers.

The higher REE abundances of the orthopyroxenes are assumed to result from refertilization via mixing with a basaltic melt from underlying depleted mantle sources. Figure 12 shows that approximately 6 to 17% refertilization by melt addition in the next step can explain the high REE abundances observed in the orthopyroxenes. In conclusion, the integration of whole-rock and mineral compositional data, coupled with comprehensive considerations of metasomatism and melting dynamics, substantially enhances our understanding of the genesis of the Kızıldağ mantle peridotites. Utilizing orthopyroxene as a key indicator of melt depletion and recognizing the secondary, metasomatic origins of clinopyroxenes, allows for a more nuanced interpretation of the mantle's melting and metasomatic history, as well as its implications for the broader tectonic framework of the Tethyan region.

Origin of metasomatic mineral phases

Anorthitic plagioclase is present in certain Kızıldağ peridotite samples adjacent to pyroxenite and gabbro veins. Pargasitic to tremolitic amphibole has been identified in samples collected both near these veins and at greater distances, suggesting that both mineral phases are products of the metasomatic alteration of pre-existing spinel peridotite due to hydrous arc melt percolation (e.g., Dijkstra et al., 2001; Tartarotti et al., 2002; Rampone and Borghini, 2008). The presence of tremolitic amphibole may indicate a distinct secondary alteration process (e.g., Schmitt and Poli, 1998; Bach et al., 2004). In contrast, pargasitic amphibole, often associated with modal metasomatism in mantle peridotites and typically found alongside phases such as phlogopite (e.g., Coltorti et al., 2007; Bénard and Ionov, 2013), supports the notion of fluid and melt infiltration.

While plagioclase can form through both low-pressure re-equilibration of spinel peridotite and melt impregnation, the characteristics observed in our samples deviate from those typical of re-equilibration. Notably, we did not identify hallmark textures such as plagioclase rims around spinel or plagioclase+orthopyroxene exsolution lamellae within clinopyroxene porphyroclasts. These textures are well-documented in regions like western Iberia and the Nain ophiolite in Iran, where they indicate re-equilibration under plagioclase stability conditions (e.g., Piccardo et al., 1993; Chazot et al., 2005; Rampone et al., 2005; Pirnia et al., 2018). The absence of these defining features reinforces the conclusion that the observed plagioclase likely crystallized from percolating melt during shallow-level metasomatic processes. Additionally, a positive linear correlation between clinopyroxene TiO_2 content and spinel TiO_2 (Fig. 10d), which aligns with the peridotite–IAT melt interaction array (Fig. 10c), provides compelling evidence for interaction with Ti-rich melts. This observation is corroborated by Ti enrichment in coexisting orthopyroxene (Fig. 10e). The secondary nature of clinopyroxene in Group-2 samples, its spatial association with amphibole, and the infrequent occurrence of plagioclase collectively imply that these minerals crystallized from Ti-rich, hydrous melts during their ascent through the mantle wedge. This interpretation is further supported by the presence of light REE-enriched orthopyroxene (relative to middle REE) in the Kızıldağ peridotites (Fig. 12), indicating later metasomatic enrichment by hydrous melts following an earlier stage of partial melting. Such processes likely facilitated significant changes within the peridotites, including the dissolution of clinopyroxene and orthopyroxene, alongside the precipitation of olivine (Piccardo, 2003). This transformation may also explain the presence of newly crystallized, Ca-enriched olivine neoblasts observed in some samples.

Experimental studies (e.g., Borghini et al., 2011) indicate a negative correlation between plagioclase anorthite content and pressure, with ~An90 plagioclase typically crystallizing at ~0.2 GPa. In contrast, pressures calculated for our samples (Mercier, 1980) exceed 1.5 GPa. This discrepancy suggests that the observed plagioclase is not in equilibrium with the original mantle assemblage, reaffirming that it likely crystallized from percolating melt during shallow-level metasomatic processes. As discussed earlier, melting initially occurred in the garnet stability field and transitioned into the spinel stability field during the early stages of subduction, as evidenced by orthopyroxene melting modeing results (Fig. 7). Rapid upwelling of the asthenospheric mantle may have resulted in faster cooling, leading to higher equilibration temperatures. However, the presence of plagioclase and amphibole poses a contradiction, as their crystallization typically requires significantly lower pressure and temperature conditions. The crystallization of plagioclase from percolating melt in the shallow mantle can enrich the residual melt in titanium, potentially increasing the TiO_2 content of spinel if sufficient equilibration occurs. In contrast, in Group-2 samples, concurrent crystallization or re-equilibration of clinopyroxene with the melt complicates this process, as clinopyroxene competes with spinel for available titanium (Fig. 10d). Despite spinel from plagioclase-bearing peridotite samples exhibiting TiO_2 content ranging from 0.16 to 0.62 wt.%, we contend that the influence of plagioclase formation on spinel TiO_2 is minimal. This conclusion stems from the negligible modal abundance of plagioclase, as well as the elevated TiO_2 concentrations found in plagioclase-free peridotite samples.

We propose that after the upwelling of the asthenospheric mantle and during the later stages of subduction initiation, fluids released from the slab could have initiated further melting in the mantle wedge. This process is likely responsible for the crystallization of plagioclase, amphibole, and clinopyroxene at shallower mantle depths. Consequently, the petrological and geochemical evidence strongly supports the assertion that the percolating metasomatic melt enriched the TiO_2 content in pre-existing spinel. This interaction led to the crystallization of Ti-rich secondary clinopyroxene (or the equilibration of primary clinopyroxene), alongside the formation of plagioclase and pargasitic amphibole in these peridotites, consistent with findings from previous research (Arai and Matsukage, 1996; Boudier and Nicolas, 1995; Koga et al., 2001; Müntener et al., 2010; Piccardo et al., 2007; Sanfilippo et al., 2013; Tamura et al., 2008).

HSE behaviour and radiogenic Os addition during SSZ-type ophiolite generation

The HSE have a strong affinity for liquid metals and sulfides (e.g., Holzheid et al., 2000) leading to their preferential partitioning into the Earth's core relative to the silicate Earth. They are also enriched in mantle sulfides compared to silicate minerals. PGE are commonly categorized by their melting temperatures: the Ir group (IPGE: Os, Ir, and Ru) has melting points exceeding 2300 °C, while the Pd group (PPGE: Rh, Pt, and Pd) has melting points below 2000 °C (Barnes, 1985). These elements are present in ultra-low concentration within the Earth's mantle, hosted primarily in accessory minerals such as base metal sulfides and platinum-group minerals (e.g., laurite and PGE-alloys) (e.g., Luguet et al., 2007). Recent studies suggest that a significant portion of the PGE budget in the mantle may be hosted within sulfide minerals. High-melting-point monosulfide solid solutions are believed to concentrate the IPGE and Rh, while low-melting-point sulfides enriched in Cu likely host the majority of Pd and Au. Platinum may exist in distinct phases, potentially including metal alloys (Alard et al., 2000; Luguet et al., 2001).

During low-degree partial melting in the mantle, low-melting-point sulfides dissolve, depleting the mantle residue of these elements and enriching the partial melts that contribute to the formation of crustal section of ophiolites. Thus, subduction-related peridotites provide an intriguing context for investigating the impact of mantle melting and metasomatism on HSE fractionation, particularly due to the significant melt depletion experienced by the mantle wedge and its frequent interaction with subduction fluids and melt.

In the Kızıldağ ophiolite, two mantle peridotite samples exhibit a positive trend from Pd to Au on the PM-normalized diagram but are depleted in Pd, Re, and Au relative to the IPGE. One of these samples (K14H) is also depleted in Pt, while the other (K24H) shows enrichment in Pt compared to Pd, Re, and Au (Fig. 8a). The HSE profiles of these two samples reflect their depleted nature, with slight modifications in incompatible Pd, Re, and Au possibly related to subsequent melt interactions in a subduction setting; the positive Pt anomaly may suggest a nugget effect from Pt-bearing phases. In contrast, sample K27H shows minimal depletion from Os to Pt, with a continuous upward trend from Pt to Au, displaying concentrations of Pd, Re, and Au nearly ten times higher than those in the other two samples (Fig. 8a). This anomaly diverges from typical depleted peridotite signatures and suggests significant addition of these elements during melt percolation in the subduction zone.

Crustal rocks and extrusives of the Kızıldağ ophiolite share similarities with mantle peridotites in their contents of Pt, Pd, Re, and Au but exhibit significantly lower levels of Os, Ir, Ru, and, in some cases, Rh (Fig. 8b). This overall positive correlation from Os to Au indicates that the formation of crustal units results from mantle melts that have undergone varying degrees of differentiation.

Rhenium exhibits moderate incompatibility, showing a strong tendency to concentrate in the melt phase during partial melting of the mantle. This leads to Re depletion in the residual solid phase and an enrichment in the melt. In contrast, Os displays high compatibility, preferentially partitioning into the solid phase during mantle melting (Burton et al., 2002). As a result, the Re/Os ratio is notably low in the residual solid phase but higher in the partial melt, with this ratio increasing as the melt undergoes further differentiation. This signature holds potential for elucidating the melting history of residual mantle in ophiolites and could even be used to date the formation of crustal sections.

Crustal section of ophiolites normally exhibits relatively low Os content (~30 ppt; Peucker-Ehrenbrink and Jahn, 2001) but have high radiogenic Os concentrations. Given that mantle peridotites contain higher Os concentrations than basaltic melts, their Os isotopic values of mantle peridotites largely remain unaffected during interaction with basaltic melts in subduction zones (Shirey and Walker, 1998). Sample K27AH, from the Group-2b mantle peridotites, has a very depleted $^{187}Os/^{188}Os$ ratio of 0.1179 and a Re-depletion age of ~1.5 Ga (Supplementary Table 5), implying long-term preservation of a refractory peridotite segment in the asthenospheric mantle. The other two peridotite samples also exhibit sub-primitive upper mantle Os isotopic compositions of 0.1203 and 0.1248, suggesting no significant modification by radiogenic Os-rich fluids/basaltic melts.

However, since melts generated during mantle melting typically have very low Os content, the incorporation of radiogenic Os from subducted oceanic crust into the mantle wedge can lead to significant variations in the $^{187}Os/^{188}Os$ ratios of the partial melt. This aspect becomes evident when examining the initial Os isotopic compositions of crustal rocks and extrusives from the Kızıldağ ophiolite. While these rocks show a positive correlation between Re/Os and $^{187}Os/^{188}Os$ ratios (Fig. 8c), most samples plot above the 94 Ma reference line, constructed based on the U-Pb zircon ages (Şimşek et al., 2023) from gabbroic cumulates, along with initial Os isotope ratios and Re/Os values of the most radiogenic peridotite sample. This positioning suggests a more radiogenic composition of crustal rocks and extrusives compared to the reference line.

Additionally, a noteworthy observation is that a significant proportion of these rocks exhibit initial Os isotopic compositions (highlighted in blue text in Fig. 8c) that are substantially higher than even the most radiogenic mantle peridotite sample (K14H; $^{187}Os/^{188}Os = 0.12475$). This finding indicates that the initial Os isotopic ratios of the crustal rocks and extrusives do not reflect the composition of their mantle source; rather, they represent a mixture of melts derived from both radiogenic Os-rich crustal components and depleted mantle-derived melts. This scenario poses challenges for dating oceanic crust using the Re-Os method suggests significant transport of ^{187}Os to the mantle wedge during subduction processes while indicating that the Os isotopic compositions of mantle rocks remain largely unaffected.

Integration of mantle processes in subduction initiation

The integrated petrographic, geochemical, and isotopic analysis of the Kızıldağ ophiolite provides unique insights into the complex interplay of mantle melting, metasomatism, and melt-rock interactions that govern subduction initiation. Our findings support a refined four-stage tectonic model (Fig. 13), rigorously constrained by multi-faceted data from across the ophiolite's crust-mantle transition, which resolves the compositional evolution of both the mantle and crustal sections:

Stage 1 (Figure 13a): Initial subduction and lithospheric foundering

This initial stage encompasses lithospheric foundering and subsequent asthenospheric upwelling, inducing decompression melting within the garnet to spinel transition zone under nominally anhydrous conditions. The melts generated are consistent with fore-arc basalt-like compositions, reflecting a predominantly asthenospheric origin with a subduction character. Importantly, this initial phase does not, on its own, generate the highly depleted mantle residues characteristic of more evolved supra-subduction zone settings; rather, it forms a distinct suite of early harzburgites exhibiting only subtle trace element signatures indicative of initial partial melting.

Stage 2 (Figure 13b): Hydrous flux melting and transition to depleted mantle

This stage marks a critical geodynamic transition wherein slab dehydration triggers hydrous flux melting within the overlying mantle wedge. The resulting influx of slab-derived fluids enhances partial melting of a mantle source exhibiting incipient depletion, thereby leading to the formation of highly-depleted Group-1 harzburgites. These residues are defined by elevated spinel Cr#, pronounced heavy REE depletion, and sub-primitive mantle $^{187}Os/^{188}Os$ (0.11795–0.12475), reflecting the key role and nature of slab fluids. Concomitantly, while slab-derived fluids enhance LILE mobility, the previously depleted character of the melt source constrains LILE enrichment. Consequently, Group-1 harzburgites retain a highly-depleted signature, indicative of a unique fluid-dominated metasomatic regime wherein slab-derived fluxes selectively drive partial melting, without substantial input from fertile asthenospheric components. This transient interplay underscores the dynamic coupling between fluid flux, mantle depletion, and the initiation of subduction processes.

Stage 3 (Figure 13c): Slab roll-back and mantle wedge metasomatism

A critical stage in mantle wedge evolution is initiated by slab roll-back, which promotes renewed asthenospheric upwelling. This, in turn, facilitates the infiltration of more fertile melts, inducing concomitant metasomatism of the previously depleted mantle wedge and giving rise to Group-2 compositions through the precipitation of secondary clinopyroxene (up to 5.5 vol.%). The trace element distributions in these newly generated compositions provide a robust record of this upwelling. In conjunction with the ascent of asthenospheric melts, which are richer in Ti and other incompatible elements, continued slab dehydration and oxidizing fluids drive significant changes in the mantle wedge. Group-2 peridotites showcase elevated heavy REE and elevated spinel TiO_2 (up to 0.87 wt.%), reflecting the significant influence of melt-rock interaction and fluid overprinting, further supported by elevated oxygen fugacity values.

Stage 4 (Figure 13d): Boninitic magmatism and Os isotope signature

The sustained influx of slab-derived fluids initiates the remelting of a previously depleted and metasomatized mantle wedge, which has been progressively enriched in LILE and hydrous components during earlier stages of subduction. This hybridized source undergoes high-degree partial melting under intensely hydrous conditions, generating boninitic melts distinguished by pronounced depletion in heavy REE, and significant enrichment in LILE. Given that the slab fluids interact with a mantle source that is inherently refractory at this stage, the resultant melts exhibit limited Ti enrichment in spinel compared to melts derived from the asthenosphere. Secondary clinopyroxene crystallizing from these melts similarly displays subdued Ti enrichment, further underscoring the unique geochemical signature of this process. The boninitic melts inherit radiogenic $^{187}Os/^{188}Os$ isotopic signatures (up to 0.28326) from subducted oceanic crust, providing robust evidence for open-system fluid flux and sediment/altered oceanic crust melting within the subduction zone. Shallow crystallization of these melts under oxidizing conditions yields precipitation of plagioclase and amphibole at various depths of depleted lithospheric mantle. These phases represent the culmination of progressive mantle wedge modification, wherein slab-derived fluids drive the remelting of refractory, metasomatized lithologies to produce distinctive subduction-initiation magmatism.

This model aligns with global supra-subduction zone (SSZ) ophiolite formation processes, particularly in the Tethyan domain. The observed REE disequilibrium between orthopyroxene and clinopyroxene (Fig. 9), particularly the concave-upward orthopyroxene/clinopyroxene ratio patterns, reflects the multi-stage nature of melting and metasomatism inferred from petrography and trace element systematics. These disequilibrium features are consistent with temporally decoupled episodes of mantle processing, as further elaborated in our four-stage subduction initiation model (Fig. 13). Early-formed orthopyroxene, residual from melting under anhydrous conditions, was variably overprinted by later percolating melts and slab-derived fluids that crystallized secondary clinopyroxene. Incomplete trace element re-equilibration between these phases during ascent preserved the record of successive mantle processes, from melt extraction to hydrous metasomatism and secondary crystallization, which together shaped the geochemical heterogeneity of the Kızıldağ mantle peridotites.

Conclusions

The geochemical and isotopic data support a four-stage model for subduction initiation, involving lithospheric foundering, hydrous flux melting, slab roll-back, and boninitic magmatism. This model aligns with global supra-subduction zone (SSZ) ophiolite formation processes, particularly in the Tethyan domain.

The Kızıldağ ophiolite mantle peridotites exhibit a wide range of pressures (1.5–3.5 GPa) and high closure temperatures (~1200–1400 °C), supporting melting in both garnet and spinel stability fields. The preservation of high-temperature mineral assemblages and the lack of extensive re-equilibration textures provide evidence for rapid upwelling, indicating a multi-stage melting process during subduction initiation. Highly depleted harzburgites (Group-1) reflect significant melt extraction, while Group-2 peridotites, despite their spinel compositions indicating a higher degree of melting, show enrichment due to metasomatic processes, highlighting the heterogeneous nature of the mantle wedge. Comparison to Oman peridotites indicates the complexities of the Tethyan ophiolite mantle wedge systems, and suggests that various melt sources and metasomatic processes played a role in generating geochemical diversity of the mantle sources for ophiolites in subduction-related systems.

The inconsistencies in melting degrees derived from spinel, orthopyroxene, and whole-rock compositions highlight the limitations of conventional melting models in metasomatized mantle systems. Orthopyroxene, with its larger grain size, is recommended for melting modeling as it (especially the core) better preserves the primary melting history. In contrast, clinopyroxene should be avoided due to its predominantly secondary origin and susceptibility to metasomatic alteration, which can obscure primary geochemical signatures. This study emphasizes the importance of integrating robust mineral proxies and multi-method approaches to accurately reconstruct mantle melting processes in subduction zones.

The mantle peridotites experienced metasomatic enrichment through interaction with boninitic and island-arc tholeiite (IAT) melts. This led to the crystallization of secondary minerals such as clinopyroxene, amphibole, and plagioclase, particularly in Group-2 peridotites. The enrichment process highlights the role of subduction-related fluids and melts in modifying mantle compositions.

Variations in Os isotope ratios ($^{187}Os/^{188}Os$) reveal the incorporation of radiogenic Os from subducding oceanic crust into the mantle wedge. This process is evident in the crustal rocks, which exhibit more radiogenic Os signatures compared to the mantle peridotites.

Group-2 peridotites exhibit elevated oxygen fugacity, directly linked to subduction-related fluids and melts. This oxidation state corroborates metasomatic enrichment and provides critical evidence for the role of slab-derived components in modifying the mantle wedge.

The integration of petrographic, geochemical, and isotopic data reveals the complex interplay between mantle melting, metasomatism, and subduction initiation in the Kızıldağ ophiolite. These findings provide a robust framework for understanding SSZ mantle evolution and contribute to the broader discourse on the dynamics of Tethyan oceanic lithosphere processes.

Acknowledgements

This study was funded by TUBITAK under project #109Y219, Scientific Research Foundation of Karadeniz Technical University (Project #9080), and the National Natural Science Foundation of China (42350001). Additionally, this research received support from the Presidential International Fellowship Initiative (PIFI) awarded by the Chinese Academy of Sciences (CAS) to IU. We thank Executive Editor Georg F. Zellmer, handling Editor Tod E. Waight, and reviewers Shoji Arai, Daniel Coulthard, and two anonymous reviewers for their insightful comments and constructive feedback, which significantly improved the manuscript.

Data availability

The data in this article are available in the article and/or in its online supplementary material, and on the EarthChem data repository with DOI: 10.60520/IEDA/113539.

Supplementary Materials

Supplementary materials include whole-rock major and trace element compositions (Suppl. Table 1), mineral major oxide compositions (Suppl. Table 2), and trace element compositions of clinopyroxene (Suppl. Table 3) and orthopyroxene (Suppl. Table 4). Additionally, the supplementary materials provide whole-rock HSE and Os isotopic compositions (Suppl. Table 5), pressure and temperature calculation (Suppl. Table 6), and the parameters used for the melting and refertilization modeling of orthopyroxene (Suppl. Table 7) from the Kızıldağ ophiolite samples. Supplementary data are available at Journal of Petrology online.

References

Agranier, A. and Lee, C.-T. A. (2007). Quantifying trace element disequilibrium during mantle melting: New insights from rare earth element partitioning in natural lherzolites. Geochemistry, Geophysics, Geosystems, 8, Q11018.

Alard, O., Griffin, W. L., Lorand, J. P., Jackson, S. E., O'Reilly, S. Y. (2000). Non-chondritic distribution of the highly siderophile elements in mantle sulphides. Nature, 407, 891-894.

Aldanmaz, E., van Hinsbergen, D. J., Yıldız-Yüksekol, Ö., Schmidt, M. W., McPhee, P. J., Meisel, T., Güçtekin, A., Mason, P. R. (2020). Effects of reactive dissolution of orthopyroxene in producing incompatible element depleted melts and refractory mantle residues during early fore-arc spreading: constraints from ophiolites in eastern Mediterranean. Lithos, 360, 105438.

Arai, S. (1994). Characterization of spinel peridotites by olivine-spinel compositional relationships: review and interpretation. Chemical Geology, 113, 191-204.

Bağcı, U., Parlak, O., Höck, V. (2005). Whole-rock and mineral chemistry of cumulates from the Kızıldağ (Hatay) ophiolite (Turkey): clues for multiple magma generation during crustal accretion in the southern Neotethyan ocean. Mineralogical Magazine, 69, 53-76.

Bağcı, U., Parlak, O., Höck, V. (2008). Geochemistry and tectonic environment of diverse magma generations forming the crustal units of the Kızıldağ (Hatay) ophiolite, Southern Turkey. Turkish Journal of Earth Sciences, 17, 43-71.

Barnes, S. J., Naldrett, A. J., Gorton, M. P. (1985). The origin of the fractionation of platinum-group elements in terrestrial magmas. Chemical Geology, 53, 303-323.

Borghini, G., Fumagalli, P., Arrigoni, F., Rampone, E., Berndt, J., Klemme, S., Tiepolo, M. (2023). Fast REE re-distribution in mantle clinopyroxene via reactive melt infiltration. Geochemical Perspectives Letters, 26, 40-44.

Brunelli, D., Seyler, M., Cipriani, A., Ottolini, L., and Bonatti, E. (2006), Discontinuous melt extraction and weak refertilization of mantle peridotites at the Vema lithospheric section Mid-Atlantic Ridge: Journal of Petroleum Science and Engineering, 47, 745–771.

Burton, K. W., Gannoun, A., Birck, J. L., Allègre, C. J., Schiano, P., Clocchiatti, R., Alard, O. (2002). The compatibility of rhenium and osmium in natural olivine and their behaviour during mantle melting and basalt genesis. Earth and Planetary Science Letters, 198, 63-76.

Chen, C., Su, B. X., Xiao, Y., Pang, K. N., Robinson, P. T., Uysal, I., Lin, W., Qin, K.-Z., Avcı, E., Kapsiotis, A. (2019). Intermediate chromitite in Kızıldağ ophiolite (SE Turkey) formed during subduction initiation in Neo-Tethys. Ore Geology Reviews, 104, 88-100.

Chen, C., Su, B. X., Xiao, Y., Uysal, İ., Lin, W., Chu, Y., Jing, J. J., Sakyi, P. A. (2020). Highly siderophile elements and Os isotope constraints on the genesis of peridotites from the Kızıldağ ophiolite, southern Turkey. Lithos, 368, 105583.

Creaser, R. A., Papanastassiou, D. A., Wasserburg, G. J. (1991). Negative thermal ion mass spectrometry of osmium, rhenium and iridium. Geochimica et Cosmochimica Acta, 55, 397-401.

Dick, H. J., Bullen, T. (1984). Chromian spinel as a petrogenetic indicator in abyssal and alpine-type peridotites and spatially associated lavas. Contributions to Mineralogy and Petrology, 86, 54-76.

Dick, H. J. B., Fisher, R. L. (1984). Mineralogic studies of the residues of mantle melting: abyssal and alpine-type peridotites. In: Developments in Petrology (Vol. 11, No. 2, pp. 295-308). Elsevier.

Dick, H. J. B. (1989). Abyssal peridotites, very slow spreading ridges and ocean ridge magmatism. Geological Society, London, Special Publications, 42, 71-105.

Dilek, Y., Thy, P. (1998). Structure, petrology and seafloor spreading tectonics of the Kizildag ophiolite, Turkey. Geological Society, London, Special Publications, 148, 43-69.

Dilek, Y., Thy, P. (2009). Island arc tholeiite to boninitic melt evolution of the Cretaceous Kizildag (Turkey) ophiolite: Model for multi-stage early arc–forearc magmatism in Tethyan subduction factories. Lithos, 113, 68-87.

Eiler, J. M., McInnes, B., Valley, J. W., Graham, C. M., Stolper, E. M. (1998). Oxygen isotope evidence for slab-derived fluids in the sub-arc mantle. Nature, 393, 777-781.

Eiler, J. M., Schiano, P., Valley, J. W., Kita, N. T., Stolper, E. M. (2007). Oxygen-isotope and trace element constraints on the origins of silica-rich melts in the subarc mantle. Geochemistry, Geophysics, Geosystems, 8, 2006GC001503.

Gamal El Dien, H., Arai, S., Doucet, L. S., Li, Z. X., Kil, Y., Fougerouse, D., Reddy, S. M., Saxey, D. W., Hamdy, M. (2019). Cr-spinel records metasomatism not petrogenesis of mantle rocks. Nature Communications, 10, 5103.

Gerya, T. (2011). Future directions in subduction modeling. Journal of Geodynamics, 52, 344-378.

Gong, X. H., Shi, R. D., Griffin, W. L., Huang, Q. S., Xiong, Q., Chen, S. S., Zhang, M., O'Reilly, S. Y. (2016). Recycling of ancient subduction-modified mantle domains in the Purang ophiolite (southwestern Tibet). Lithos, 262, 11-26.

Gong, X. H., Shi, R. D., Xu, J. F., Huang, Q. S., Su, B. X. (2020). ‘Garnet’ lherzolites in the Purang ophiolite, Tibet: Evidence for exhumation of deep oceanic lithospheric mantle. Geophysical Research Letters, 47, e2019GL086101.

Guillot, S., Hattori, K. (2013). Serpentinites: Essential roles in geodynamics, arc volcanism, sustainable development, and the origin of life. Elements, 9, 95-98.

Gurnis, M., Hall, C., Lavier, L. (2004). Evolving force balance during incipient subduction, Geochemistry, Geophysics, Geosystems, 5, 1-31.

Hellebrand, E., Snow, J. E., Dick, H. J., Hofmann, A. W. (2001). Coupled major and trace elements as indicators of the extent of melting in mid-ocean-ridge peridotites. Nature, 410, 677-681.

Hellebrand, E., Snow, J. E., Mühe, R. (2002). Mantle melting beneath Gakkel Ridge (Arctic Ocean): abyssal peridotite spinel compositions. Chemical Geology, 182, 227-235.

Holzheid, A., Sylvester, P., O'Neill, H. S. C., Rubie, D. C., Palme, H. (2000). Evidence for a late chondritic veneer in the Earth's mantle from high-pressure partitioning of palladium and platinum. Nature, 406, 396-399.

Ionov, D. A., Bodinier, J. L., Mukasa, S. B., Zanetti, A. (2002). Mechanisms and sources of mantle metasomatism: major and trace element compositions of peridotite xenoliths from Spitsbergen in the context of numerical modelling. Journal of Petrology, 43, 2219-2259.

Ishii, T., Sato, H., Haraguchi, S., Fryer, P., Fujioka, K., Bloomer, S., Yokose, H. (2000). Petrological characteristics of peridotites from serpentinite seamounts in the Izu-Ogasawara-Mariana Forearc. Journal of Geography (Chigaku Zasshi), 109, 517-530.

Jean, M. M., Shervais, J. W., Choi, S. H., Mukasa, S. B. (2010). Melt extraction and melt refertilization in mantle peridotite of the Coast Range ophiolite: an LA–ICP–MS study. Contributions to Mineralogy and Petrology, 159, 113-136.

Jean, M. M. and Shervais, J. W. (2017). Melt extraction and melt refertilization in the mantle wedge: Evidence from chromite-hosted melt inclusions and Cr-spinel chemistry in the Coast Range ophiolite. Journal of Petrology, 58, 1145–1171.

Johnson, K. T., Dick, H. J., Shimizu, N. (1990). Melting in the oceanic upper mantle: an ion microprobe study of diopsides in abyssal peridotites. Journal of Geophysical Research: Solid Earth, 95, 2661-2678.

Johnson, K. T., Dick, H. J. (1992). Open system melting and temporal and spatial variation of peridotite and basalt at the Atlantis II fracture zone. Journal of Geophysical Research: Solid Earth, 97, 9219-9241.

Karaoğlan, F., Parlak, O., Klötzli, U. R. S., Thoeni, M., Koller, F. (2013). U–Pb and Sm–Nd geochronology of the Kızıldağ (Hatay, Turkey) ophiolite: implications for the timing and duration of suprasubduction zone type oceanic crust formation in the southern Neotethys. Geological Magazine, 150, 283-299.

Kelemen, P., Yogodzinski, G., Scholl, D. (2003). Along-strike variation in the Aleutian island Arc genesis of high Mg# andesite and implications for continental crust. In J. Eiler (Ed.), Geophysical Monograph Series (Vol. 138, pp. 223-276). Americal Geophysical Union. https://doi.org/10.1029/138GM11.

Kinzler, R. J. (1997). Melting of mantle peridotite at pressures approaching the spinel to garnet transition: application to mid-ocean ridge basalt petrogenesis. Journal of Geophysical Research: Solid Earth, 102, 853-874.

Liang, Y. (2003). Kinetics of crystal-melt reaction in partially molten silicates: 1. Grain scale processes. Geochemistry, Geophysics, Geosystems, 4, 2002GC000375.

Lin, K. Y., Wang, K. L., Chung, S. L., Bingöl, A. F., Iizuka, Y., Lee, H. Y. (2020). Tracking the magmatic response to subduction initiation in the forearc mantle wedge: Insights from peridotite geochemistry of the Guleman and Kızıldağ ophiolites, Southeastern Turkey. Lithos, 376, 105737.

Liu, T., Wu, F. Y., Liu, C. Z., Eyuboglu, Y., Zhu, D. C., Zhang, C., Ji, W.B., Xu, Y., Zhang, Z. Y. (2020). Testing oceanic crust–mantle decoupling by Sr–Nd–Hf–Os isotopes of Neo-Tethyan ophiolites. Lithos, 376, 105757.

Luguet, A., Alard, O., Lorand, J. P., Pearson, N. J., Ryan, C., O’Reilly, S. Y. (2001). Laser-ablation microprobe (LAM)-ICPMS unravels the highly siderophile element geochemistry of the oceanic mantle. Earth and Planetary Science Letters, 189, 285-294.

Luguet, A., Shirey, S. B., Lorand, J. P., Horan, M. F., Carlson, R. W. (2007). Residual platinum-group minerals from highly depleted harzburgites of the Lherz massif (France) and their role in HSE fractionation of the mantle. Geochimica et Cosmochimica Acta, 71, 3082-3097.

Luguet, A., Nowell, G. M., Pearson, D. G. (2008). ^{184}Os/^{188}Os and ^{186}Os/^{188}Os measurements by Negative Thermal Ionisation Mass Spectrometry (N-TIMS): Effects of interfering element and mass fractionation corrections on data accuracy and precision. Chemical Geology, 248, 342-362.

Lytwyn, J. N., Casey, J. F. (1993). The geochemistry and petrogenesis of volcanics and sheeted dikes from the Hatay (Kizildag) ophiolite, southern Turkey: Possible formation with the Troodos ophiolite, Cyprus, along fore-arc spreading centers. Tectonophysics, 223, 237-272.

Maffione, M., van Hinsbergen, D. J., de Gelder, G. I., van der Goes, F. C., Morris, A. (2017). Kinematics of Late Cretaceous subduction initiation in the Neo-Tethys Ocean reconstructed from ophiolites of Turkey, Cyprus, and Syria. Journal of Geophysical Research: Solid Earth, 122, 3953-3976.

Meisel, T., Walker, R. J., Irving, A. J., Lorand, J. P. (2001). Osmium isotopic compositions of mantle xenoliths: a global perspective. Geochimica et Cosmochimica Acta, 65, 1311-1323.

Moazzen, M., Ahangari, M., Oberhänsli, R., Altenberger, U. (2024). Mineral chemistry and alteration patterns of Cr-spinel in serpentinized peridotites from NW Iran. Journal of Asian Earth Sciences: X, 11, 100178.

Müntener, O., Manatschal, G. (2006). High degrees of melt extraction recorded by spinel harzburgite of the Newfoundland margin: The role of inheritance and consequences for the evolution of the southern North Atlantic. Earth and Planetary Science Letters, 252, 437-452.

Niu, Y. (1997). Mantle Melting and Melt Extraction Processes beneath Ocean Ridges: Evidence from Abyssal Peridotites. Journal of Petrology, 38, 1047-1074.

Niu, Y. (2004). Bulk-rock major and trace element compositions of abyssal peridotites: implications for mantle melting, melt extraction and post-melting processes beneath mid-ocean ridges. Journal of Petrology, 45, 2423-2458.

Ottley, C. J., Pearson, D. G., Irvine, G. J. (2003). A routine method for the dissolution of geological samples for the analysis of REE and trace elements via ICP-MS. Plasma source mass spectrometry: Applications and Emerging Technologies, 288, 221.

Ozawa, K., Shimizu, N. (1995). Open-system melting in the upper mantle: Constraints from the Hayachine-Miyamori ophiolite, northeastern Japan. Journal of Geophysical Research: Solid Earth, 100, 22315-22335.

Palandri, J. L., Reed, M. H. (2004). Geochemical models of metasomatism in ultramafic systems: Serpentinization, rodingitization, and sea floor carbonate chimney precipitation. Geochimica et Cosmochimica Acta, 68, 1115-1133.

Palme, H., O'Neill, H.St.C. (2004). Cosmochemical estimates of Mantle Composition. In: Treatise on Geochemistry. Holland, H.D. and Turrekian, K.K. (Editors), Elsevier, Amsterdam, The Netherlands. 2, 1-38.

Pan, Q. Q., Xiao, Y., Su, B. X., Robinson, P. T., Li, W. J., Wang, J., Liu, X. (2024). Tracing material transport during subduction inception: Insights from potassium isotopes in the crustal sequence of the Troodos ophiolite. Geochimica et Cosmochimica acta, 373, 259-270.

Parkinson, I. J., Pearce, J. A. (1998). Peridotites from the Izu–Bonin–Mariana forearc (ODP Leg 125): evidence for mantle melting and melt–mantle interaction in a supra-subduction zone setting. Journal of Petrology, 39, 1577-1618.

Pearce, N. J., Perkins, W. T., Westgate, J. A., Gorton, M. P., Jackson, S. E., Neal, C. R., Chenery, S. P. (1997). A compilation of new and published major and trace element data for NIST SRM 610 and NIST SRM 612 glass reference materials. Geostandards Newsletter, 21, 115-144.

Pearce, J. A., Barker, P. F., Edwards, S. J., Parkinson, I. J., Leat, P. T. (2000). Geochemistry and tectonic significance of peridotites from the South Sandwich arc–basin system, South Atlantic. Contributions to Mineralogy and Petrology, 139, 36-53.

Peucker-Ehrenbrink, B., Jahn, B. M. (2001). Rhenium-osmium isotope systematics and platinum group element concentrations: Loess and the upper continental crust. Geochemistry, Geophysics, Geosystems, 2, 2001GC000172.

Potts, R. O., Guy, R. H. (1992). Predicting skin permeability. Pharmaceutical Research, 9, 663-669.

Pouchou, J. L., Pichoir, F. (1991). Quantitative analysis of homogeneous or stratified microvolumes applying the model “PAP”. In Electron probe quantitation (pp. 31-75). Boston, MA: Springer US.

Rampone, E., Borghini, G., Basch, V. (2020). Melt migration and melt-rock reaction in the Alpine-Apennine peridotites: Insights on mantle dynamics in extending lithosphere. Geoscience Frontiers, 11, 151-166.

Reagan, M. K., Ishizuka, O., Stern, R. J., Kelley, K. A., Ohara, Y., Blichert-Toft, J., Bloomer, S. H., Cash, J., Fryer, P., Hanan, B. B., Hickey-Vargas, R., Ishii, T., Kimura, J.I., Peate, D. W., Rowe, M. C., Woods, M. (2010). Fore-arc basalts and subduction initiation in the Izu–Bonin–Mariana system. Geochemistry, Geophysics, Geosystems, 11, Q03X12.

Reagan, M. K., Heaton, D. E., Schmitz, M. S., Pearce, J. A., Shervais, J. W., Koppers, A. P. (2019). Forearc ages reveal extensive short–lived and rapid seafloor spreading following subduction initiation. Earth and Planetary Science Letters, 506, 520-529.

Reagan, M. K., Pearce, J. A., Shervais, J. W., Christeson, G. L. (2023). Subduction initiation as recorded in the Izu-Bonin-Mariana forearc. Earth-Science Reviews, 246, 104573.

Rivalenti, G., Vannucci, R., Rampone, E., Mazzucchelli, M., Piccardo, G. B., Piccirillo, E. M., Bottazzi, P., Ottolini, L. (1996). Peridotite clinopyroxene chemistry reflects mantle processes rather than continental versus oceanic settings. Earth and Planetary Science Letters, 139, 423-437.

Ruan, T., Bai, Z-J., Zhu, W-G., Zheng, S-J. (2025). Multi-stage partial melting and melt metasomatism in the formation of the Luobusa ophiolite (Southern Tibet). Journal of Asian Earth Sciences, 277, 106394.

Salters, V. J., Stracke, A. (2004). Composition of the depleted mantle. Geochemistry, Geophysics, Geosystems, 5, Q05B07.

Sano, S., Kimura, J. I. (2007). Clinopyroxene REE geochemistry of the Red Hills peridotite, New Zealand: interpretation of magmatic processes in the upper mantle and in the Moho transition zone. Journal of Petrology, 48, 113-139.

Scott, J. M., Liu, J., Pearson, D. G., Waight, T. E. (2016). Mantle depletion and metasomatism recorded in orthopyroxene in highly depleted peridotites. Chemical Geology, 441, 280-291.

Seyler, M., Toplis, M. J., Lorand, J. P., Luguet, A., Cannat, M. (2001). Clinopyroxene microtextures reveal incompletely extracted melts in abyssal peridotites. Geology, 29, 155-158.

Shirey, S. B., Walker, R. J. (1998). The Re-Os isotope system in cosmochemistry and high-temperature geochemistry. Annual Review of Earth and Planetary Sciences, 26, 423-500.

Stern, R. J., Reagan, M., Ishizuka, O., Ohara, Y., Whattam, S. (2012). To understand subduction initiation, study forearc crust: To understand forearc crust, study ophiolites. Lithosphere, 4, 469-483.

Su, B. X., Chen, C., Xiao, Y., Robinson, P. T., Liu, X., Wang, J., Uysal, I., Bai, Y., Sun, Y., (2021). The critical role of fluid-mediated diffusion in anomalous Fe-Mg-O isotope fractionations in ultramafic rocks of ophiolites. Journal of Geophysical Research-Solid Earth, 126, e2020JB020632.

Su, B. X., Pan, Q. Q., Xiao, Y., Jing, J. J., Robinson, P. T., Uysal, I., Liu, X., Liu, J. G. (2023). Mantle peridotites of ophiolites rarely preserve reliable records of paleo-oceanic lithospheric mantle. Earth-Science Reviews, 244, 104544.

Su, B. X., Uysal, I., Akmaz, R. M., Pan, Q. Q., Demir, Y., Ackerman, L., Robinson, P. T. (2025). Chromite as a key player on highly siderophile elements and osmium isotope compositions of the refractory mantle. Geochimica et Cosmochimica Acta, doi:10.1016/j.gca.2025.04.026.

Şimşek, E., Parlak, O., Robertson, A. H. (2023). Ion-probe (SIMS) U-Pb geochronology and geochemistry of the Upper Cretaceous Kızıldağ (Hatay) ophiolite: Implications for supra-subduction zone spreading in the Southern Neotethys. Geosystems and Geoenvironment, 2, 100165.

Tekeli, O., Erendil, M. (1986). Kızıldağ Ofiyolitinin (Hatay) Jeoloji ve Petrolojisi. MTA Bullettin, 107, 33-48.

Uenver-Thiele, L., Woodland, A. B., Seitz, H. M., Downes, H., Altherr, R. (2017). Metasomatic processes revealed by trace element and redox signatures of the lithospheric mantle beneath the Massif Central, France. Journal of Petrology, 58, 395-422.

Uysal, I., Kaliwoda, M., Karsli, O., Tarkian, M., Sadiklar, M. B., Ottley, C. J. (2007). Compositional variations as a result of partial melting and melt–peridotite interaction in an upper mantle section from the Ortaca area, southwestern Turkey. The Canadian Mineralogist, 45, 1471-1493.

Uysal, I., Saka, S., Ersoy, E. Y., Bağcı, U., Kaliwoda, M., Ottley, C., Brauns, M., Şen, A. D., Köprübaşı, N., Rızaoğlu, T. (2012a). Kızıldağ ophiolite (S-Turkey): Melting and interaction processes, and Re-Os geochronology. 65th Geological Congress of Turkey, 02-06 April, pp344-347.

Uysal, I., Ersoy, E. Y., Karslı, O., Dilek, Y., Sadıklar, M. B., Ottley, C. J., Tiepolo, M., Meisel, T. (2012b). Coexistence of abyssal and ultra-depleted SSZ type mantle peridotites in a Neo-Tethyan Ophiolite in SW Turkey: Constraints from mineral composition, whole-rock geochemistry (major–trace–REE–PGE), and Re–Os isotope systematics. Lithos, 132, 50-69.

Uysal, I., Şen, A. D., Ersoy, E. Y., Dilek, Y., Saka, S., Zaccarini, F., Escayola, M., Karslı, O. (2014). Geochemical make-up of oceanic peridotites from NW Turkey and the multi-stage melting history of the Tethyan upper mantle. Mineralogy and Petrology, 108, 49-69.

Völkening, J., Walczyk, T., Heumann, K. G. (1991). Osmium isotope ratio determinations by negative thermal ionization mass spectrometry. International Journal of Mass Spectrometry and Ion Processes, 105, 147-159.

Walter, M. J. (2003). Melt extraction and compositional variability in mantle lithosphere. Treatise on Geochemistry, 2, 568.

Warren, J. M. (2016). Global variations in abyssal peridotite compositions. Lithos, 248, 193-219.

Wu, K., Yuan, H. L., Lyu, N., Peng, Z. L. (2020). The behavior of fluid mobile elements during serpentinization and dehydration of serpentinites in subduction zones. Acta Petrologica Sinica, 36, 141-153 (in Chinese with English abstract).

Xiao, Y., Teng, F. Z., Su, B. X., Hu, Y., Zhou, M. F., Zhu, B., Shi, R. D., Huang, Q. S., Gong, X. H., He, Y. S. (2016). Iron and magnesium isotopic constraints on the origin of chemical heterogeneity in podiform chromitite from the Luobusa ophiolite, Tibet. Geochemistry, Geophysics, Geosystems, 17, 940-953.

Zhou, M. F., Zhao, J. H., Jiang, C. Y., Gao, J. F., Wang, W., Yang, S. H. (2009). OIB-like, heterogeneous mantle sources of Permian basaltic magmatism in the western Tarim Basin, NW China: implications for a possible Permian large igneous province. Lithos, 113, 583-594.

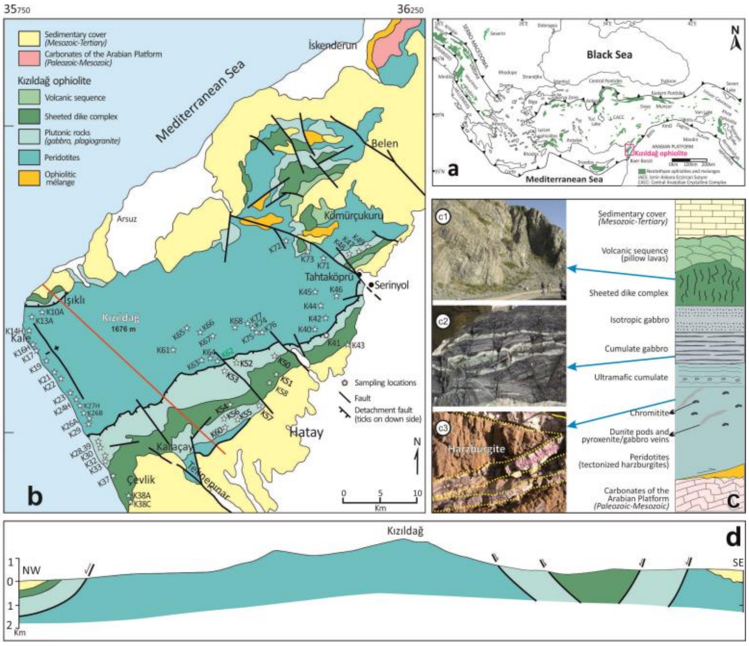

Figure 1. (a) Major tectonic units and the distribution of ophiolites in the Eastern Mediterranean region, showing the location of the Kızıldağ ophiolite. (b) Geological map of the Kızıldağ ophiolite (Dilek and Thy, 2009) in southern Türkiye, showing the distribution of various lithological units and major faults within the region. Field photographs (c1-c3) and a columnar section (c) depict the stratigraphy of the Kızıldağ ophiolite, which comprises sedimentary cover, volcanic sequences, sheeted dike complexes, ultramafic cumulates, and mantle peridotites. These units were thrust over the NW Arabian plate during the late Cretaceous. (d) Structural cross-section of the Kızıldağ ophiolite.

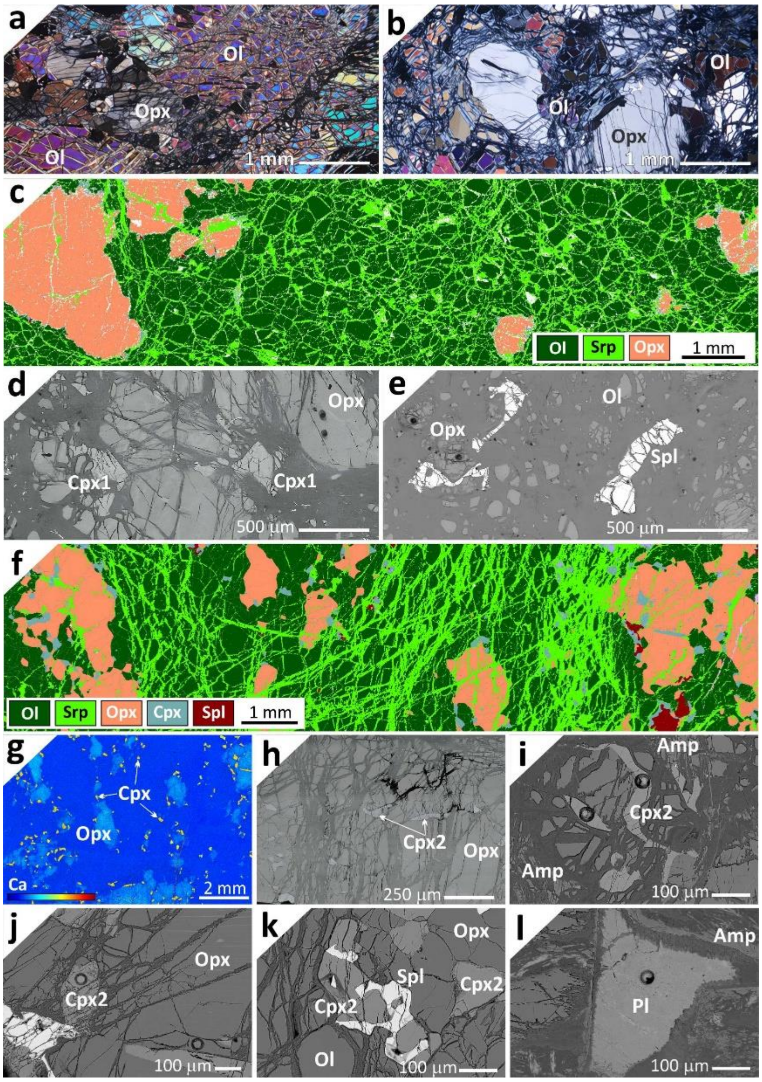

Figure 2. Microstructures of Group-1 (experienced minimal modal metasomatism) and Group-2 (modal metasomatized) peridotites, focusing on the textural relationships between primary and secondary phases as revealed by various analytical techniques. (a, b) Representative photomicrographs of Group-1 peridotites in cross-polarized light, illustrating the modal mineralogy and textural relationships. The textures are predominantly porphyroclastic, with large, deformed olivine (Ol) porphyroclasts exhibiting undulose extinction and kink bands, set in a matrix of finer-grained neoblasts formed by dynamic recrystallization. Orthopyroxene (Opx) is also present as both porphyroclasts, sometimes showing alteration to bastite serpentine, and smaller, more equant grains. (c) TESCAN Integrated Mineral Analyzer (TIMA) phase map of a Group-1 peridotite, showing the spatial distribution of major phases and secondary alteration products. Note the pervasive serpentinization along grain boundaries and within olivine grains. (d, e) Back-scattered electron (BSE) images of Group-1 peridotites revealing microstructural details. (d) Primary clinopyroxene (Cpx1) is present as relatively large grains, often located in close proximity to orthopyroxene (Opx) or between orthopyroxene and olivine (Ol) grains. (e) An orthopyroxene (Opx) grain is present, exhibiting a relatively homogeneous composition in BSE. Adjacent olivine grains show varying degrees of alteration to serpentine minerals, with the alteration concentrated along fractures and grain boundaries. The spinel (Spl) displays an anhedral morphology. (f) TIMA phase map of a Group-2 peridotite (modal metasomatized), showing the spatial distribution of major phases and secondary clinopyroxenes. Note the pervasive serpentinization along grain boundaries and within olivine and orthopyroxene grains. (g) TIMA elemental map of a Group-2 peridotite showing the distribution of Ca, highlighting the presence and distribution of secondary clinopyroxene (Cpx2) within the peridotite. The occurrence of this secondary clinopyroxene suggests its addition to the mantle peridotite, potentially during melt percolation, resulting in modal metasomatism. (h-l) BSE images of Group-2 peridotites illustrating the occurrence of secondary phases. (h) Worm-like secondary clinopyroxene (Cpx2) is present, often located close to large orthopyroxene grains or interstitial to orthopyroxene and olivine grains. (i) Amphibole (Amp) is associated with secondary clinopyroxene (Cpx2), potentially representing a crystallization product from melt percolation within the peridotite. (j) Secondary clinopyroxene (Cpx2) is located interstitial to orthopyroxene (Opx) and in close proximity to spinel (Spl). (k) Secondary clinopyroxene (Cpx2) is associated with spinel (Spl), and is also present interstitial to olivine and at the contact between olivine and orthopyroxene. (l) Plagioclase (Pl) is associated with amphibole (Amp), potentially representing a crystallization product from the percolating melt during metasomatism.

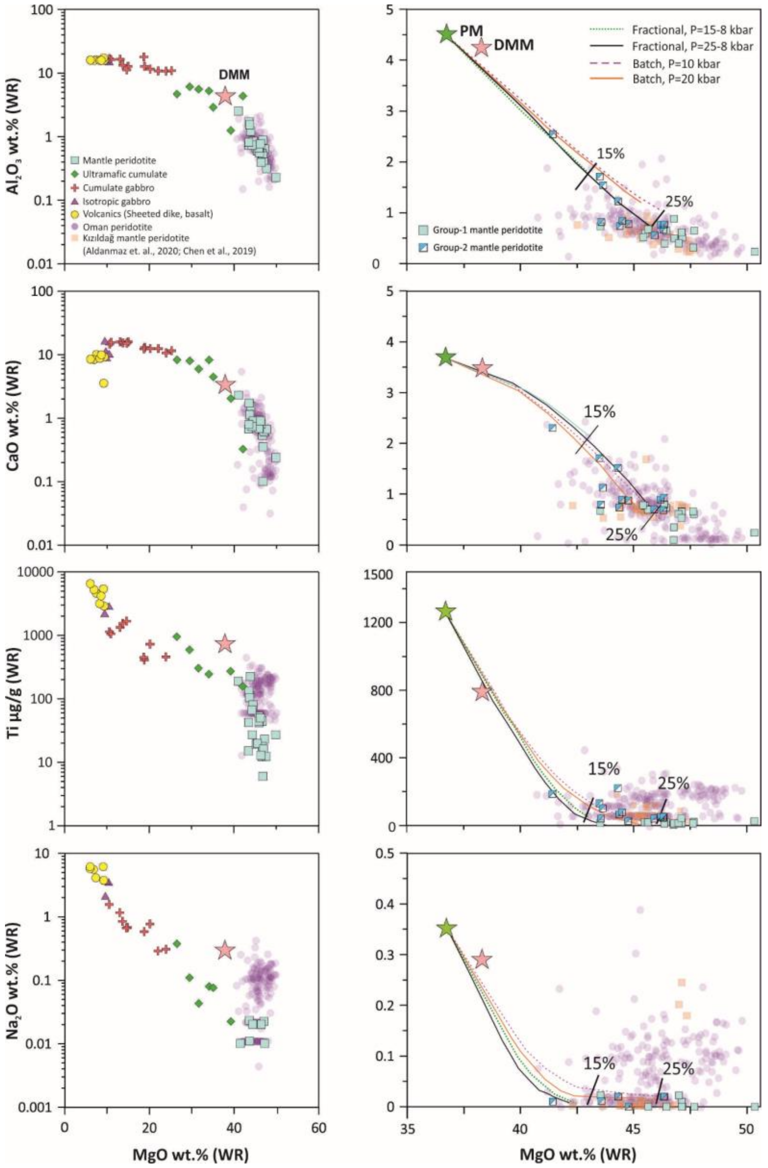

Figure 3. Whole-rock (WR) major and trace element variation diagrams (Al2O3, CaO, Ti, Na2O) versus MgO for samples from the Kızıldağ ophiolite, compared to primitive mantle (PM; Palme and O'Neill, 2004) and depleted MORB mantle (DMM; Salters and Stracke, 2004) compositions. For comparison, calculated melting residues are plotted for both isobaric batch melting (at 10 and 20 kbar) and near-fractional decompression melting (28–8 kbar and 15–8 kbar) following the models of Niu (1997). Oman data are also shown for comparison and are from Kourim et al. (2022), Hanghøj et al. (2010), and Monnier et al. (2006).

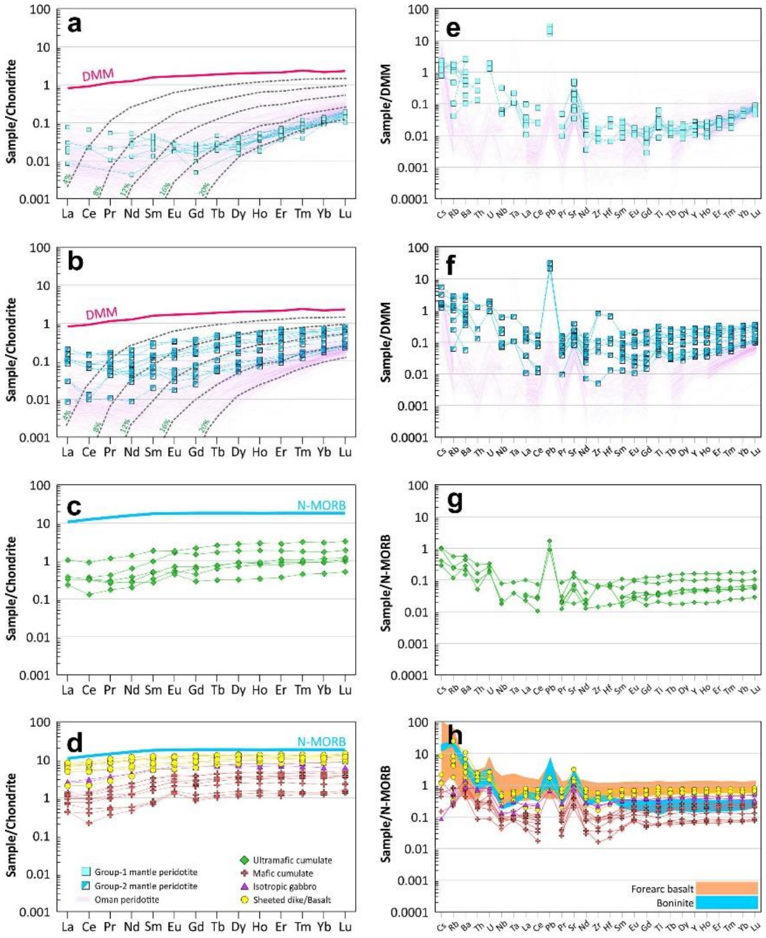

Figure 4. Chondrite-normalized REE patterns (a-d) and DMM-normalized (e, f) and N-MORB-normalized (g, h) trace element patterns for mantle peridotites (a, b and e, f) and crustal rocks and extrusives (c, d and g, h) of the Kızıldağ ophiolite. Compositional variations of fore-arc basalt and boninite (Reagan et al., 2010) are included for comparison. Panels a, b, e, and f compare the REE and multi-element patterns of Oman peridotites (Kourim et al., 2022; Hanghøj et al., 2010; Monnier et al., 2006) with the Kızıldağ samples. Fractional non-modal melting curves (4 to 20%), calculated using partition coefficients from Kelemen et al. (2003) and melting reaction modes from Kinzler (1997) are shown in panels (a) and (b). DMM refers to Depleted MORB mantle (Salters and Stracke, 2004), whereas chondrite REE abundances as well as N-MORB values are sourced from Sun and McDonough (1989).

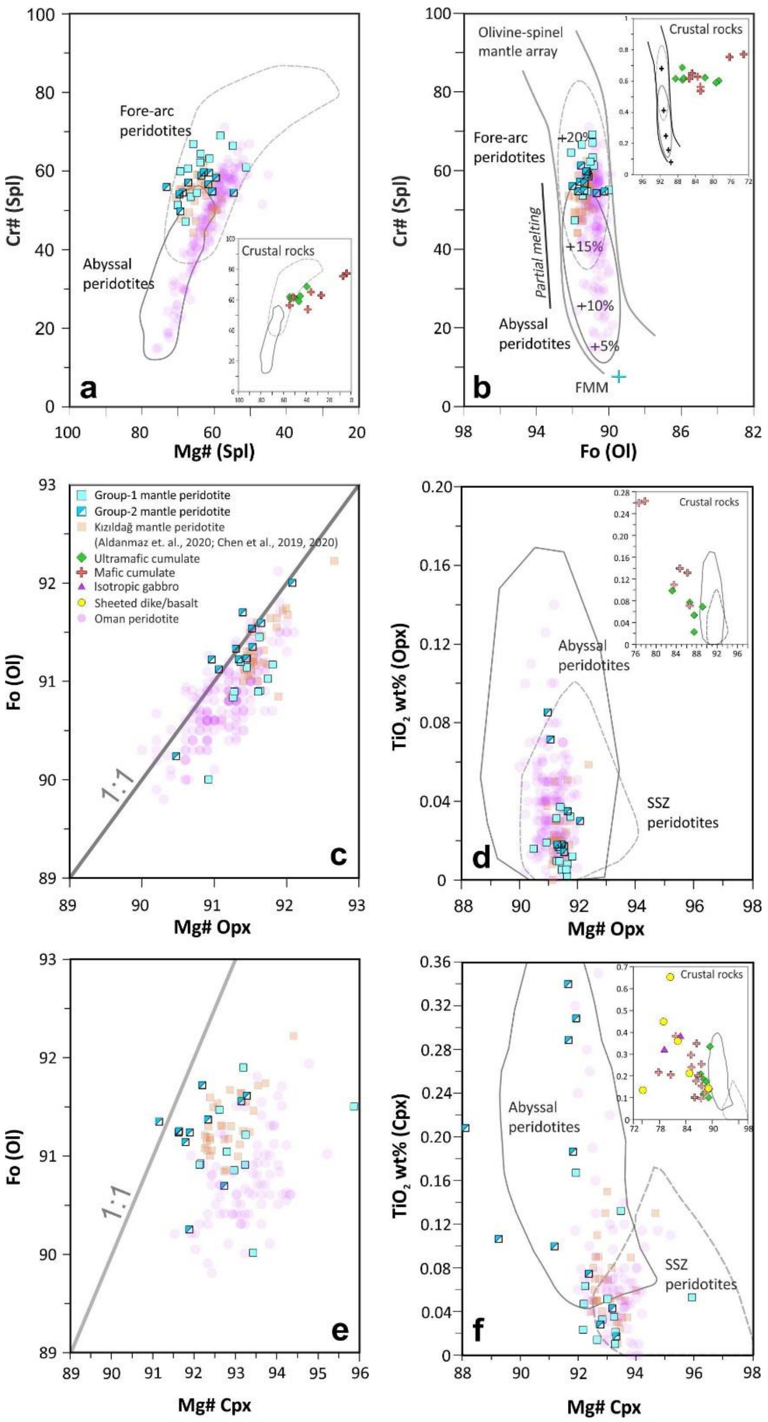

Figure 5. Compositional variations of various phases from the mantle peridotite and crustal rock samples, as well as extrusives (data for the crustal rocks and extrusives are shown in inset diagrams) of the Kızıldağ ophiolite. (a) Cr# versus Mg# for spinel, and (b) Cr# values of spinel versus Fo contents of coexisting olivine depicted on the olivine-spinel mantle array (OSMA) diagram of Arai (1994). Degrees of melting shown in OSMA are calculated from the equation proposed by Hellebrand et al. (2001). (c, e) Co-variation of olivine Fo contents with (c) orthopyroxene and (e) clinopyroxene Mg# for the Group-1 and Group-2 mantle peridotite samples. (d, f) TiO2 contents versus Mg# of (a) orthopyroxene and (b) clinopyroxene. Data for the mantle peridotites are compared to established fields for abyssal and SSZ-related peridotites. Data for abyssal and SSZ-related peridotites for (a) and (b) are sourced from Pearce et al. (2000) and Ishii et al. (1992). Orthopyroxene (d) and clinopyroxene (f) compositions for abyssal peridotites are derived from Hamlyn and Bonatti (1980), Shibata and Thompson (1986), Dick (1989), Johnson et al. (1990), Edwards et al. (1996), and Hellebrand et al. (2002), while those for SSZ-related peridotites are based on Ishii et al. (1992), Parkinson et al. (1992), Parkinson and Pearce (1998), and Pearce et al. (2000). Oman data are shown for comparison and sourced from Kourim et al. (2022), Hanghøj et al. (2010), and Monnier et al. (2006).

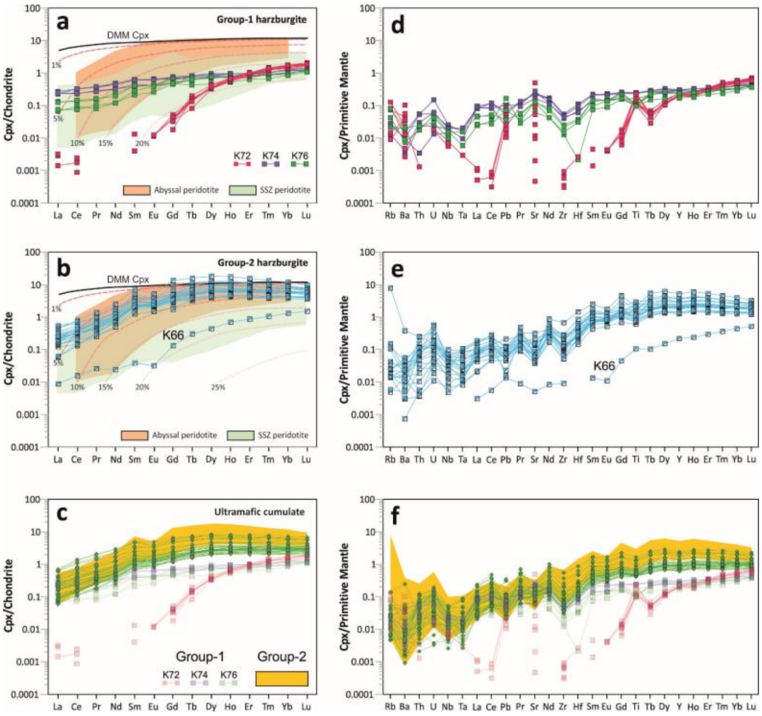

Figure 6. Chondrite-normalized REE (a, b) and PM-normalized trace element patterns (d, e) for clinopyroxene from Group-1 (a, d) and Group-2 (b, e) mantle peridotites. (c) and (f) shows the chondrite and PM-normalized REE and trace patterns for clinopyroxene of ultramafic cumulates, respectively. Thin pink dashed lines in (a) and (b) show the composition of residual clinopyroxene calculated for 1 to 20% non-modal fractional melting of spinel peridotites. The calculations use melting parameters from Johnson et al. (1990) and Sano and Kimura (2007), with the composition of the DMM clinopyroxene (Workman and Hart, 2005) indicated by the thick black line. The abyssal peridotite field is adapted from Brunelli et al. (2006), whereas the field for SSZ-peridotites is referenced from Ruan et al. (2025). Chondrite values are sourced from Sun and McDonough (1989) and PM values are from Palme and O’Neill (2004).

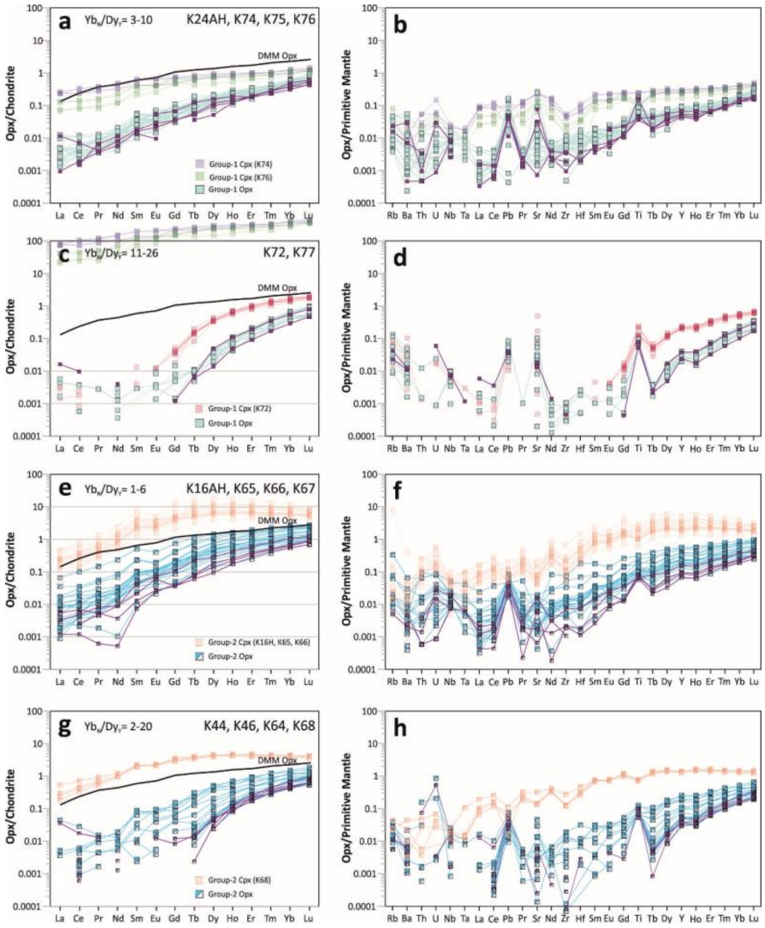

Figure 7. Chondrite-normalized REE (a, c, e, g) and PM-normalized (b, d, f, h) trace element patterns for orthopyroxene from Group-1 (a-d) and Group-2 (e-h) mantle peridotite samples of the Kızıldağ ophiolite, grouped by their YbN/DyN ratios. (a, b) display data with YbN/DyN ratios between 3 and 10; (c, d) with YbN/DyN ratios between 11 and 26; (e, f) with YbN/DyN ratios between 1 and 6; and (g, h) with YbN/DyN ratios between 2 and 20. Specific sample names are indicated for each group. The composition of the DMM orthopyroxene (Workman and Hart, 2005) is indicated by the thick black line. The purple symbols indicate the most depleted orthopyroxene in each sample. Composition of primary clinopyroxene from Group-1 samples and secondary clinopyroxene in Group-2 samples are shown on (a-d) and (e-h) for comparison. Chondrite values are sourced from Sun and McDonough (1989) and PM values are from Palme and O'Neill (2004).

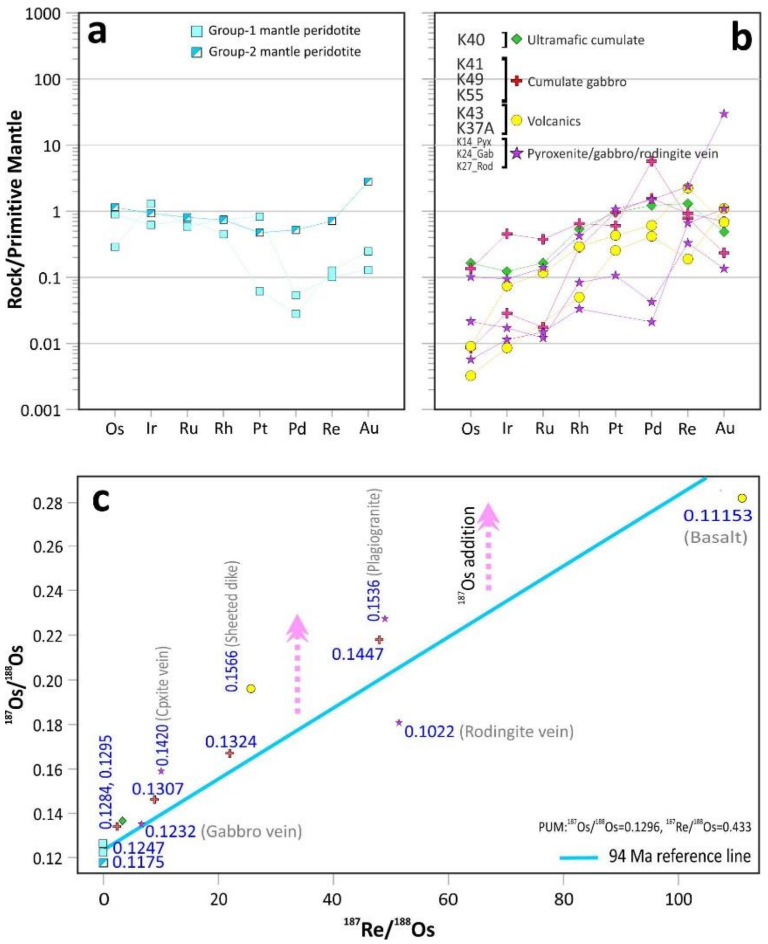

Figure 8. (a, b) PM-normalized HSE patterns for various lithological units of the Kızıldağ ophiolite, including Group-1 and Group-2 mantle peridotites (a), as well as ultramafic cumulates, mafic cumulates, volcanics, and pyroxenite, rodingite, and plagiogranite veins (b). (c) Plot of 187Os/188Os versus 187Re/188Os for samples from the Kızıldağ ophiolite, compared to 94 Ma reference line. Values indicated in blue text represent the initial 187Os/188Os values for individual samples calculated back to 94 Ma. PM values are sourced from Palme and O'Neill (2004).

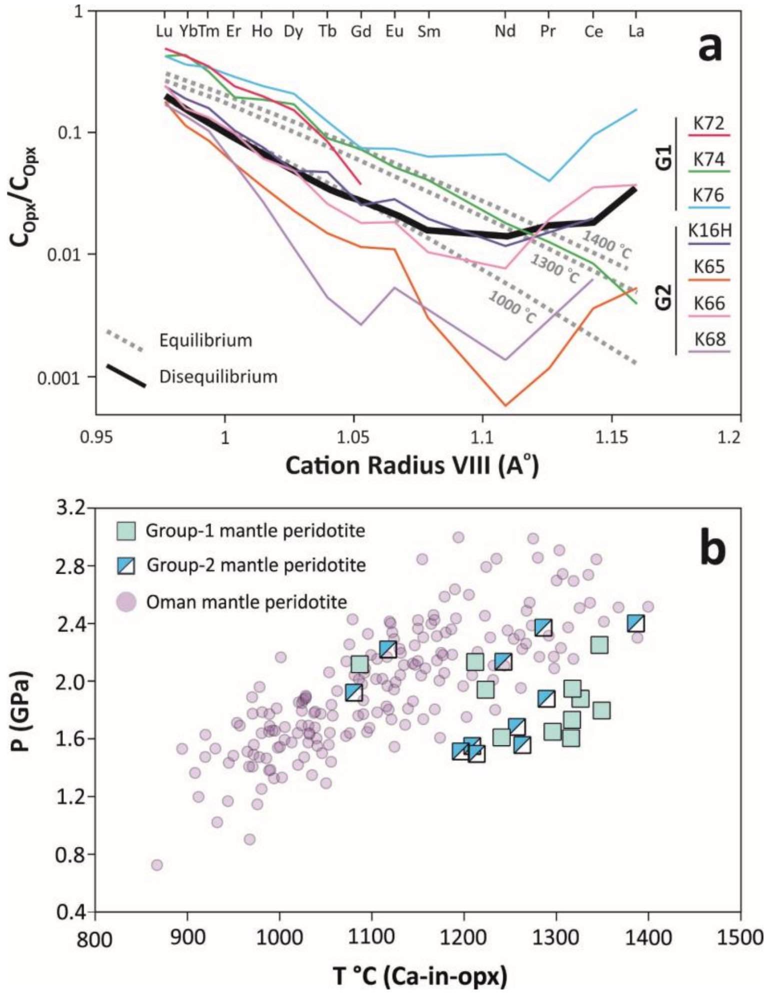

Figure 9. (a) Plot of COpx/CCpx REE ratios versus trivalent cation radius for selected Kızıldağ peridotite samples. Gray dashed lines show equilibrium partitioning curves (Agranier and Lee, 2007) at different temperatures; the upward convex trends of most samples indicate disequilibrium. (b) Variation of pressures (P) and temperatures (T oC) calculated from orthopyroxene compositions for the Kızıldağ mantle peridotites. P and T data for the Oman ophiolite, calculated from orthopyroxene compositions based on datasets from Kourim et al. (2022), Hanghøj et al. (2010) and Monnier et al. (2006), are shown for comparison.

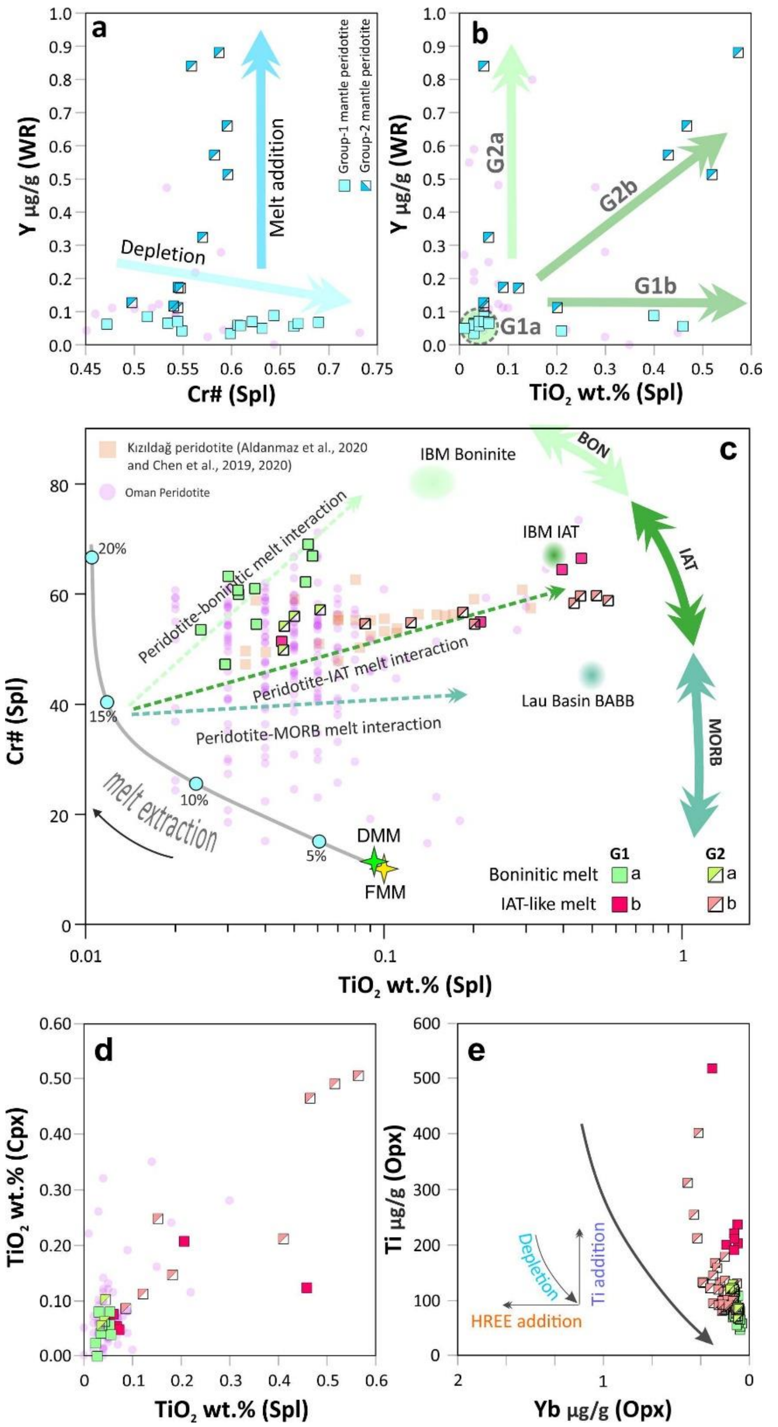

Figure 10. (a) Plot of whole-rock Y content versus Cr# in spinel for Group-1 and Group-2 mantle peridotites, illustrating melt addition and depletion trends. (b) Plot of whole-rock Y versus TiO2 in spinel for the same peridotite groups, highlighting various enrichments of Ti and Y. (c) Cr# versus TiO2 diagram for spinels (Pearce et al., 2000) from the Kızıldağ mantle peridotites, showing distinct trends between partial melting and melt-peridotite interaction. IBM: Izu-Bonin-Mariana, BON: boninite, IAT: island-arc tholeiite, BABB: Back-arc basin basalt, MORB: mid-oceanic ridge basalt, FMM: fertile MORB mantle, DMM: depleted MORB mantle. (d) Plot of TiO2 in clinopyroxene versus TiO2 in spinel. (e) Plot of Ti versus Yb in orthopyroxene. Oman data are from Kourim et al. (2022), Hanghøj et al. (2010), and Monnier et al. (2006).

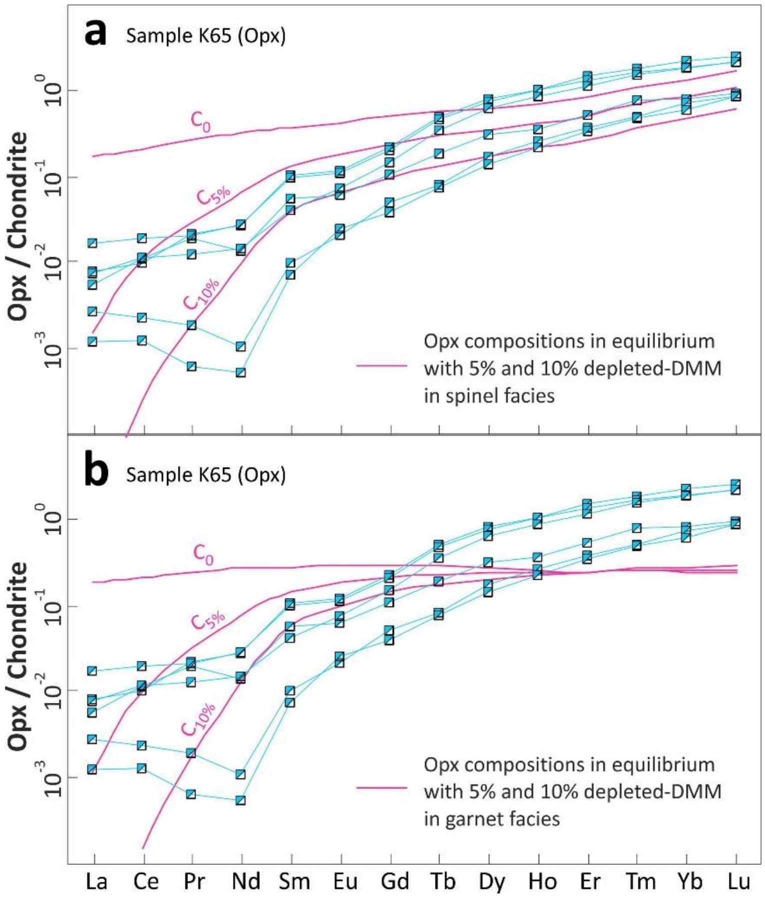

Figure 11. REE abundances of the orthopyroxenes from the sample K65 are compared with model orthopyroxene compositions, which are in equilibrium with the residual mantle after 5% and 10% closed-system fractional melting of the depleted MORB mantle source (DMM; Salters and Stracke, 2004). Model orthopyroxene compositions calculated for (a) spinel and (b) garnet lherzolite assemblages (ol0.55(-0.22) + opx0.25(0.38) + cpx0.18(0.71) + sp0.02(0.13) and ol0.55(0.08) + opx0.20(-0.19) + cpx0.15(0.81) + gt0.10(0.30), respectively; Sano and Kimura, 2007). The partition coefficients (Kd) utilized in our models are sourced from Sano and Kimura (2007). Note that both models fail to reproduce the REE patterns of the sample K65.

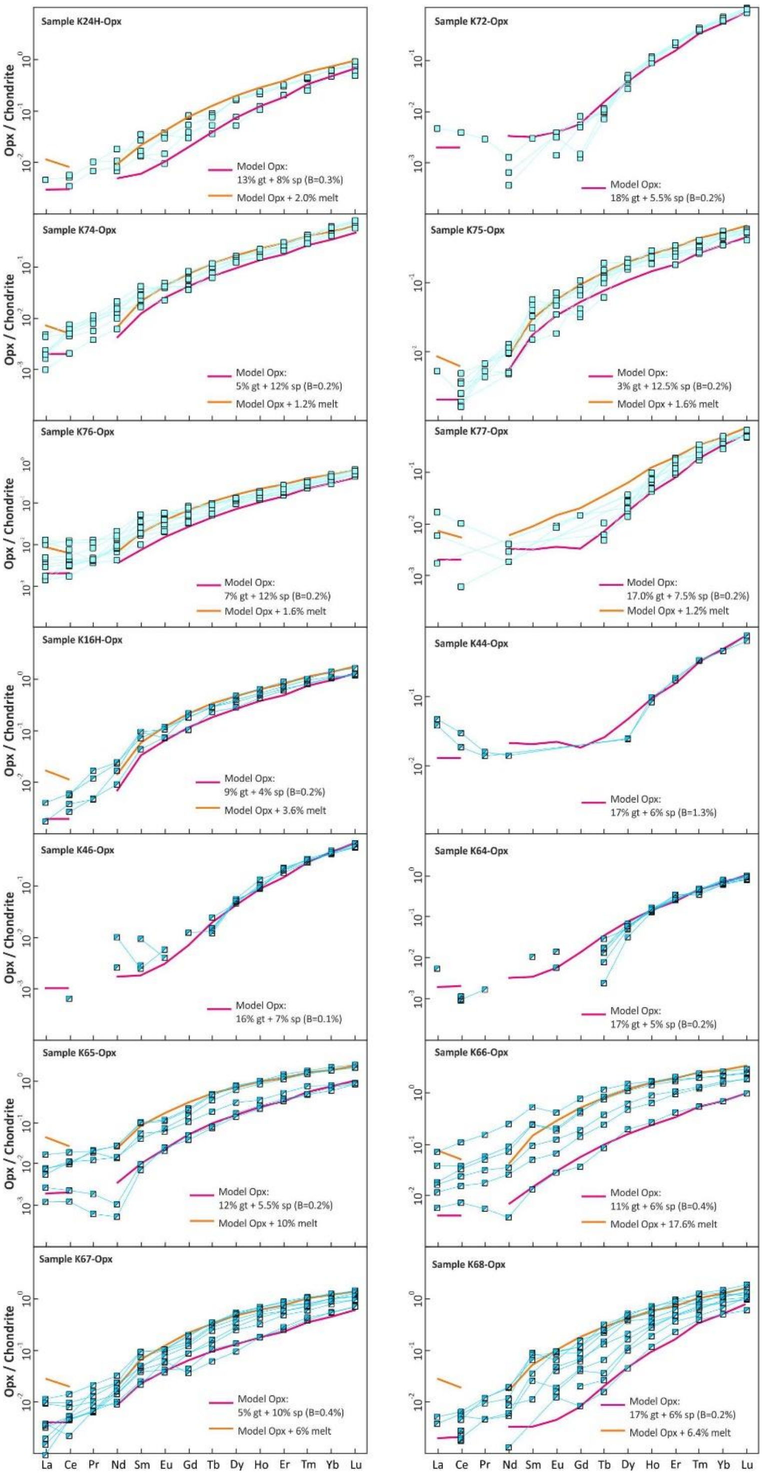

Figure 12. REE abundances of the orthopyroxenes in sample K65 compared with melting (in purple) and refertilization (in orange) models. The purple lines represent the REE abundances of orthopyroxenes in equilibrium with two-stage depleted mantle (garnet followed by spinel facies). The orange lines indicate the enrichment in orthopyroxene through melt interaction, calculated using simple mixing models, reflecting significant variations in REE abundances. Note that the REE abundances of the orthopyroxenes increase from core to rim. Further details regarding the geochemical modelling are provided in the main text.

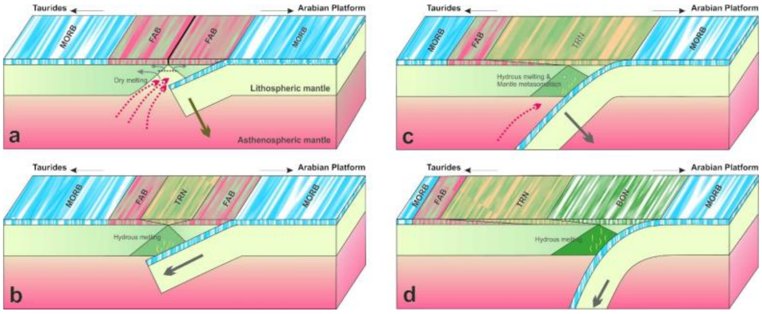

Figure 13. Cartoon model illustrating the magmatic processes associated with subduction initiation, demonstrating a range of compositional variability within the Kızıldağ ophiolite. (a) The initial stage of subduction is marked by the detachment and sinking of buoyant lithospheric material into the asthenosphere. This process triggers passive upwelling of the asthenospheric mantle, leading to decompression melting and the generation of low-degree melts characterized by fore-arc basalt (FAB) geochemical signatures. At this early stage, the interaction between these FAB-like melts and the overlying mantle peridotite is typically limited, preserving the depleted nature of the mantle. (b) As subduction progresses, fluids released from the dehydrating subducting oceanic crust migrate into the overlying mantle wedge. These fluids induce melting within the FAB-depleted mantle residue, resulting in the generation of melts with transitional (TRN) geochemical characteristics. These melts exhibit compositional signatures intermediate between those of MORB-like melts, reflecting the depleted source, and boninitic melts, influenced by the addition of slab-derived components. (c) The onset of slab rollback is a critical event that leads to the upwelling of deeper asthenospheric mantle. This upwelling generates a new pulse of relatively Ti-rich melts. As this Ti-rich melt percolates through the overlying mantle wedge, it interacts with the previously depleted peridotites. This interaction leads to the crystallization of secondary phases, including clinopyroxene, amphibole, and, in some cases, minor plagioclase, at varying depths within the lithospheric mantle. This process results in modal metasomatism, enriching the depleted mantle in these secondary phases. (d) In the later stages of subduction initiation, fluids and melts derived directly from the descending slab induce high-degree melting of the harzburgitic mantle. This process generates boninitic melts, which are characterized by high MgO contents and enrichment in large ion lithophile elements (LILE), reflecting the influence of slab-derived fluids.